



Flame resistance of geopolymer foam coatings for the fire protection of steel

Johan Sarazin, Catherine Davy, Serge Bourbigot, Grégory Tricot, Jérôme Hosdez, David Lambertin, Gaelle Fontaine

► To cite this version:

Johan Sarazin, Catherine Davy, Serge Bourbigot, Grégory Tricot, Jérôme Hosdez, et al.. Flame resistance of geopolymer foam coatings for the fire protection of steel. Composites Part B: Engineering, 2021, Composites Part B: Engineering, 222, pp.109045. 10.1016/j.compositesb.2021.109045 . hal-03272136

HAL Id: hal-03272136

<https://hal.univ-lille.fr/hal-03272136>

Submitted on 13 Jun 2023

HAL is a multi-disciplinary open access archive for the deposit and dissemination of scientific research documents, whether they are published or not. The documents may come from teaching and research institutions in France or abroad, or from public or private research centers.

L'archive ouverte pluridisciplinaire **HAL**, est destinée au dépôt et à la diffusion de documents scientifiques de niveau recherche, publiés ou non, émanant des établissements d'enseignement et de recherche français ou étrangers, des laboratoires publics ou privés.



Distributed under a Creative Commons Attribution - NonCommercial 4.0 International License

Flame resistance of geopolymer foam coatings for the fire protection of steel

Johan Sarazin¹, Catherine A. Davy^{2,*}, Serge Bourbigot^{1,3}, Grégory Tricot⁴,

Jérôme Hosdez⁵, David Lambertin⁶, Gaëlle Fontaine^{1,*}

*Corresponding authors, email: catherine.davy@centralelille.fr, gaelle.fontaine@univ-lille.fr

1: Univ. Lille, CNRS, INRAE, Centrale Lille, UMR 8207 - UMET – Unité Matériaux et Transformations, F-59000 Lille, France

2 : Univ. Lille, CNRS, Centrale Lille, ENSCL, Univ. Artois, UMR 8181 - UCCS - Unité de Catalyse et de Chimie du Solide, Lille F-59000, France

3: Institut Universitaire de France (IUF)

4: Univ. Lille, CNRS, UMR 8516 - LASIRE – Laboratoire de Spectroscopie pour les Interactions, la Réactivité et l'Environnement, F-59000 Lille, France

5: Univ. Lille, CNRS, Centrale Lille, Laboratoire de Mécanique, Multiphysique et Multiéchelle (LaMcube) UMR CNRS 9013, Lille 59000, France

6: CEA DEN, DE2D, SEAD, LCBC, F-30207 Bagnols sur Cèze, France

Highlights :

- Novel GP foams based on MK+SF are formulated and characterized for fire resistance
- H₂O₂ and CTABr foam stabilizing agent provide a controlled porosity of 81%
- GP foams provide superior fire protection to steel in a burn-through scenario
- The amount of GP cement only decreases from 60-68% to 53-58% after fire test
- Due to SF expansion, heat conductivity of foams is reduced by a factor of 2

Abstract: This research investigates the fire resistance of novel geopolymer (GP) foams, based on alkali-activated metakaolin and silica fume (SF). Fresh GP foams are applied as coatings on steel plates. After one week curing, the foams are subjected to a flame burn-through test. Changes in their physico-chemical properties are characterized before and after fire test, mainly with XRD, quantitative MAS NMR, electron probe micro-analysis, quantitative X ray micro-computed tomography and heat conductivity. Results show that GP foams are excellent thermal barriers, providing up to 251°C less than for uncoated steel plate. Their porosity ranges between 25 and 81%, for typical pore sizes d_{50} from 0.5 to 3.0 mm. ^{29}Si MAS NMR shows that the proportion of GP cement only decreases from 60-68% to 53-58% after fire. SF expands and creates small pores in the coating, which is favorable to decrease heat conductivity by a factor of 2 whatever the foam.

Keywords: Temperature, Stability, Alkali Activated Cement, Silica Fume, Refractory Cement

1- Introduction

Despite decades of investigations, the fire protection of civil engineering structures is still the subject of ongoing research [1-3]. In particular, steel structures may collapse and involve huge human and economic loss.

In case of a fire, intumescent coatings act as passive protections by lowering the maximum steel temperature below standard critical values [4-6]. A number of such materials has been studied, mainly organic intumescent materials, or cement-based materials [1,6-11]. Organic coatings do not last long in a fire (they are usually limited to 2 hours), and at high temperature, they may even contribute to combustion reactions and generate toxic gases in enclosed areas (e.g. corridors or tunnels) [3,6-7]. Inorganic cement-based materials are relevant candidates for passive fire protection of steel structures due to their thermal barrier property, high thermal resistance, durability, wear-resistance, low cost and good adhesion to concrete and steel.

Among such cement-based materials, geopolymers are relevant for high temperature applications [12-17]. They are obtained by the chemical activation of solid alumino-silicate powdered precursors, mainly metakaolin (MK), ground granulated blast furnace slag (GGBFS), fly ash or silica fume (SF), used alone or as mixes [18-24]. The significant literature available shows that *novel* formulations can still be proposed in the context of fire resistance, as follows.

Indeed, to improve fire protection, GP foams exist, which use MK-based GP cements [3,9,25-30]. These GP foams are either acid- or alkali- activated. Although acid-based GP foams exhibit better mechanical strength [25], thermal stability [31] and fire resistance [30], alkali-activated GP foams are easier to handle and manufacture on the industrial scale, and their durability is better known [9, 32].

Let first discuss the choice of the adequate solid precursor for fire resistance. Indeed, a number of authors indicate an insufficient thermal stability of MK-based GP cements [33-38]. However, Hammel et al. [8] propose MK-based GP, which resists to both fire and water; the GP is made out of a mix of MK and silica powder. The authors indicate an optimal (Si/Al) ratio of 18-20, but they use a peculiar silica powder with a $\text{SiO}_2/\text{AlO}_2$ in a mole ratio of 27/1. According to Barbosa et al. [39], MK-based GP cements activated with sodium silicate are able to display remarkable thermal stability, provided that they are cured and dried at 65°C, and added with a small amount of glycerol to limit micro-cracking upon drying. An excellent thermal performance of potassium K alkali-activated MK, compared to Na, is also found in the literature [40].

Other solid precursors have been investigated as candidates for thermal resistance, e.g. Na- or K-alkali activated Class F fly ash [6,11,18, 41-43], potentially added with MK [44], but they display significant shrinkage and strength loss in the range 800-1200°C. Alkali-activated blends of MK and GBFS are also proven as excellent cements for limited drying shrinkage and thermal resistance [36], although they combine both aluminosilicate geopolymer ‘gel’ structure (sodium aluminum silicate hydrates N-A-S-H) and Ca- and Na-rich Al-substituted silicate hydrates (C(N)-A-S-H) [45]. The addition of GBFS into MK-based cement is thought to modify the nanostructure of N-A-S-H, therefore improving their thermal stability over 800°C.

In a similar manner, for Yang et al. [46], adding fly ash to alkali-activated MK increases the geopolymer (Si/Al) ratio (from 1.4 to 1.6), leads to a more compact binding gel and induces smaller drying shrinkage. When searching for optimal mechanical strength and compactness, Nmiri et al. [47] have determined a molar ratio ($\text{SiO}_2/\text{Al}_2\text{O}_3$) of 3.84 for MK-based GP added with silica fume. According to Sarkar et al. [48], optimal mechanical performance of MK-

based GP added with colloidal silica is obtained with a sodium silicate activation, at a (Si/Al) ratio of 2.18, which is similar to the optimum ratio of 1.90 found out by Duxson et al. [49] for MK-based GP activated with varying sodium silicate solutions.

More specifically, bulk GP cements for fire resistance have been proposed by Villaquiran-Cacedo et al. [50], by activating MK and SF with potassium silicate at a molar ratio $(\text{SiO}_2/\text{Al}_2\text{O}_3) = 2.5$; the authors obtain excellent fire resistance for 0.5-0.6 cm thick pastes subjected to a fire flame. Cheng et al. [51] have developed potassium alkali-activated GP with GGBFS, as 1cm thick pastes and exposed to 1100°C flame, which have reached only 450°C on the back side after a 30 mins test. Watolla et al. [10] propose fire protective coatings made of a GP cement mixing MK and microsilica (representing 38%wt of the cement solids) and yielding a (Si/Al) molar ratio of 3.25. Their cements are based on a formulation by Krivenko et al. [32], and they are characterized by furnace-heating experiments only; the cements are not foamed specifically to optimize fire resistance.

The addition of inert fillers to brittle cements can also reduce shrinkage due to thermal constraints [37,52], e.g. alumina, quartz sand, crushed electrical porcelain or fired brick, ceramic spheres, etc. [39], but their presence limits the workability of the fresh paste.

For improved fire resistance, foamed materials are an asset. Owing to an increased void content, the heat conductivity of foams is lower than that of bulk materials. Aluminum powder and hydrogen peroxide H_2O_2 are known as successful foaming agents adapted to GP, thanks to the formation of gas bubbles in the fresh paste [9,18, 29-30, 43, 53-55]. H_2O_2 is generally preferred to Al because it releases oxygen slowly, inducing more homogeneously distributed bubbles, instead of strongly and quickly-formed dihydrogen (in presence of Al). According to Hajimohammadi et al. [55], using sodium hydroxide promotes quicker

decomposition of H_2O_2 , compared to sodium silicate. The latter promotes a more continuous H_2O_2 decomposition and foaming.

Other investigations propose sodium peroxide Na_2O_2 [3] or silica fume as porogen agents [10, 56]. Indeed, silica fume contains small amounts of silicon Si, which are able to oxidize and promote slow H_2 gas formation in highly alkaline media. According to Prudhomme et al. [56], in order to achieve significant pore systems, silica fume needs to be used to a minimal proportion of 50%wt.

Moreover, once bubbles are formed in the GP cement, they form open or closed porous systems. The foam morphology can be controlled by the cement paste rheology, and/or with varied stabilizing agents [57]. According to Bell and Kriven [9], in potassium-based GP, H_2O_2 induces closed porosity, whereas Al powder promotes open bubbles. The latter is more suited to limit shrinkage and cracks upon heating. In order to enhance open-porosity systems and stabilize the voids in H_2O_2 -GP foams, several authors have proposed to use anionic organic surfactants (such as Sodium dodecyl sulfate $\text{CH}_3(\text{CH}_2)_{11}\text{SO}_4\text{Na}$ i.e. SDS) [3, 58], cationic organic surfactants such as cetyltrimethyl ammonium bromide CTABr ($\text{CH}_3(\text{CH}_2)_{15}\text{N}(\text{Br})(\text{CH}_3)_3$) [22], non ionic organic polymer surfactants (such as Polysorbate 80 i.e. Tween 80, or Polyoxyethylene octyl phenyl ether- $(\text{C}_2\text{H}_4\text{O})_n\text{C}_{14}\text{H}_{22}\text{O}$ i.e. Triton X-100) [25-26, 28], proteins (e.g. albumen from egg whites) [28] or cheaper vegetable oils [59-60]. In particular, Petlitckaia and Poulesquen [29] have compared ionic and non ionic surfactants, and obtained homogeneous foams with minimal mechanical strength only with ionic CTABr and SDS compounds. Closed porosity systems, which are favorable to slow water release under temperature, are obtained with CTABr, whereas SDS promotes open and percolating pore systems. The type of activator also plays a role in the open or closed form of the pores [61].

Aims and scopes. Following the existing literature, the originality of this research is to investigate the fire resistance of novel GP cement foams (as in [29]), but based on mixtures of alkali-activated MK and silica fume, with a high Si/Al ratio of 3.2 (as in [10]). H₂O₂ is used as a porogen agent and a cationic surfactant (CTABr) as foam stabilizer. Three formulations are compared, a reference GP (mixing MK+SF) without H₂O₂ and CTABr, a GP foam (n.1) with H₂O₂ only, and a GP foam (n.2) incorporating both H₂O₂ and CTABr.

To assess their fire performance, the three GP pastes are applied as a coating on a steel plate, cured in a hermetic bag for one week and subjected to a flame burn through experiment at 1100°C. Extensive physico-chemical characterization is performed before and after fire experiment, X-Ray Diffraction (XRD), Magic Angle Spinning Nuclear Magnetic Resonance MAS NMR (²³Na, ²⁷Al and ²⁹Si), electron probe micro-analysis, quantitative X ray micro-Computed Tomography (microCT) and thermal conductivity to determine the performance of each coating and understand the mechanisms of fire protection.

2- Materials and methods

2.1- Materials

For comparison purposes, a reference GP coating is used, with a similar formulation to the K1b reference presented in Ref. [10], and using a stoichiometry of 6.4 SiO₂· 1 Na₂O· 1 Al₂O₃· 13.5H₂O. A high (Si/Al) molar ratio ensures fire resistance [7,17], while a limited (H₂O/Na₂O) contributes to the homogeneity of the foam bubbles brought by silica fume and H₂O₂ (see below) [55]. Foam bubbles stabilization and homogeneity is also provided by using sodium silicate as an alkaline activator, coupled to a surfactant (see below). For all formulations, the same metakaolin powder (Argical M1000, Imerys, France), silica fume (Condensil, France), sodium silicate solution (Betol 39T, Woellner, Germany), sodium

hydroxide pellets (purity of 99%, Sigma Aldrich) are used. Their chemical composition is quantified by X ray fluorescence (Table 1) to ensure exact GP formulation.

Two GP foams (n.1 and n.2) are formulated as steel fire protection coatings, with the same stoichiometry as the reference GP. For the latter, no specific foaming agent is used, but the presence of silica fume, analogous in its chemical composition to microsilica (Table 1), induces a foaming effect. For both GP foams n.1 and n.2, 2%wt foaming agent (hydrogen peroxide H_2O_2 at a concentration of 30%wt) is incorporated. One foam is made without stabilizing agent (GP foam n.1), and the other (GP foam n.2) uses a surfactant (CetylTrimethyl Ammonium Bromide, $CH_3 (CH_2)_{15} N (Br) (CH_3)_3$, or CTABr, Sigma-Aldrich) to stabilize the O_2 bubbles formed in the fresh GP paste, at the same proportion of 0.05%wt as in [29].

For each formulation, the chemical composition of sodium silicate is adjusted and mixed with NaOH pellets, and let to cool down to ambient temperature. Whenever needed, CTABr is mixed with the liquid activating sodium silicate solution. Dry MK and silica fume powders are mixed until homogeneity, before the sodium silicate solution is poured on them. The GP paste is mixed using a planetary DAC 400.2 VAC-P Speedmixer (CosSearch GmbH, Germany) mixer. H_2O_2 is added to the mix after the GP paste is homogenized.

All GP coatings are deposited at constant mass as a layer of a few millimeters on a 3 mm thick sandblasted steel plate. Each coating is let to harden and age in a hermetic bag, at ambient temperature, for one week (7 days). Each coating composition and exact sample mass is provided in Table 1. The total number of samples is also provided. Six samples have been necessary for GP foam n.1, in order to document the repeatability of the burn-through fire test. Three samples have been made for the two other formulations.

2.2- Methods

Description of burn-through fire tests. In previous research [62], a versatile fire test has been developed with a complete set of instrumentation to investigate the fire behavior of coating materials. This test is a burn-through test, which is designed to mimic the aeronautical (jet fuel) fire test defined in the ISO2685:1998 standard. In this work, this test is used to evaluate the fire resistance of geopolymer coatings, and how they contribute to protect steel and to avoid reaching its failure temperature (of around 550-600°C).

The equipment (Fig. 1) comprises the following elements: (i) a Propane burner from Bullfinch; (ii) High purity propane supplied by Air Liquide (N35, purity 99.95%); (iii) a Propane flowrate-meter from Bronkhorst High-tech; (iv) a water-cooled calorimeter from Sequoia (v) a cooling thermostat from Lauda Brinkmann (Lauda Proline RP845), (vi) an InfraRed (IR) camera from FLIR SystemsTM (ThermovisionTM A40M Researcher) calibrated from 0°C to 1000°C and (vii) fireproof panels composed of 10 mm thick calcium silicate from Final Advanced Materials (Calsil). The burner delivers a propane-air flame characterized by a heat flux of up to 200kW/m². The burner is placed at 85 mm from the coated plate, and the heat flux is calibrated at 116 kW/m² (error less than 5%). The flame temperature is measured with thermocouples at 1100°C.

During the experiment, the temperature profile is measured on a steel plate covered by a black paint, having a known emissivity of 0.95, with the IR camera. The mass loss of each coating after deposition, after one week curing and after fire test, and its thickness after one week curing (before fire test), are also determined.

X-Ray Diffraction. The method is described in detail in Appendix 1. It has been applied to MK and SF, and to the three GP formulations before and after fire test.

Solid state MAS NMR (^{29}Si , ^{23}Na and ^{27}Al). The method is described in detail in Appendix 1. It has been applied to the three GP formulations, before and after fire test.

Electron probe micro-analysis. The method is described in detail in Appendix 1. It has been applied to the three GP formulations, before and after fire test.

X ray micro-Computed Tomography (micro-CT). Six image series are acquired and processed by X ray micro-CT at the ISIS4D platform (Lille, France) [63-66]. Each image series corresponds to one different sample of GP foam (reference, foam n.1 and foam n.2) after 7 days curing, and observed before or after fire test, see Table 3. For all of them, an identical voxel size of 6.75 microns is used. Details on the setting parameters are given in Appendix 1.

Before quantitative analysis, all images are cropped in a (X, Y) plane so that sample boundaries and exterior are removed. The remaining image volumes, ranging between 26.2 and 63.8 mm³, are given in Table 3. For each given formulation, volumes of similar sizes are selected. They are chosen in order to provide representative pore structures of the materials, with a number of segmented pores of several hundreds and more.

The images are filtered and segmented with the ImageJ software [67], in a minimal manner to avoid information loss. The grey level histogram is only spread over the whole 0-255 available range. Thresholding is then performed using the image stack histogram, by selecting the local minimum grey level value between darker pores and lighter solids. This provides realistic binary images (with pores in black and the rest in white). Further, the pore size distribution is quantified as in [68], with the Beat plugin [69] for 2D Discrete Pore Size Distributions (DPSD).

Thermal conductivity. The heat conductivity of GP foams is measured by the Hot Disk thermal constants analyzer (TPS2500, Sweden) from Thermoconcept (Bordeaux, France). It is based on the transient plane source method. Data are acquired at room temperature. The condition for the heat pulse power and duration is adjusted for each sample to have optimized response parameters, and to ensure measurement reliability.

3- Results

3.1- Fire test results

Test repeatability. During the burn-through fire test, the temperature is measured at the back of two different uncoated steel plates, or at the back of a steel plate coated with GP foam n.1 (Figure 2a). Three different steel plates, each coated with GP foam n.1, are tested in order to assess the repeatability of the experiment. The maximum temperature measured on each test with the GP foam is respectively of 221.2, 219.2 and 220.5°C, compared to 640°C +/-5 for steel plate alone. This means that the temperature curves for the steel plates are similar, with a maximum difference of 10°C between the two. Comparatively, with GP foam n.1 coating, the temperature profiles are superimposed to less than 1°C during the whole experiment. This evidences the excellent test repeatability in presence of a GP coating. In the following, it is assumed that a similar repeatability is present for the other GP coatings tested.

Fire resistance of GP coatings. Table 2 shows the mass changes of the GP coatings due to curing alone, and then due to the fire test. The maximum mass loss is obtained with the reference GP, without specific foaming provided by H₂O₂. Reference GP loses 22% mass during curing, compared to 7.0 or 2.1% for foams n.1 and 2. This means that under identical curing conditions, water is very possibly released more easily from the reference GP than from the foams. After fire test, GP foam 2 (i.e. with CTABr stabilization of the foam) loses

the least mass, with 32.5% (% of the initial mass), compared to 34% for GP foam 1 and 38% for reference GP. Let now analyze whether it is also the best formulation for fire resistant.

Figure 2b compares the temperature profiles during the burn-through tests for the three different GP coatings. Whatever the coating considered, the temperature rise is lower than for the uncoated steel plates. The maximum decrease in temperature (-251°C) is obtained with GP foam n.2, whereas the lowest (-122°C) is obtained with the reference GP. This means that GP foaming provides a better thermal barrier than bulk GP. The addition of foam-stabilizing CTABr enhances the thermal barrier effect, with a temperature difference of 48°C compared to GP foam n.1 (without CTABr). However, Table 2 shows that CTABr also increases the foam thickness, from 5.5 mm (GP foam n.1) to 10.7 mm (GP foam n.2).

Moreover, a temperature plateau is observed at 100°C . It is attributed to free water release from the GP coatings. This plateau is more pronounced with GP foams than with reference GP, possibly because the reference GP has already lost more water during curing (with a mass loss of 22% for reference GP and only 7 and 2.1% for foams 1 and 2 respectively).

3.2- Physico-chemical characterization

3.2.1- GP cement structure

XRD results. X ray diffractograms are determined first for the raw MK and silica fume (SF) powders, and compared to reference GP after one week curing and before fire test (Figure 3). The presence of quartz in MK significantly flattens its spectrum, so that its amorphous content is not clearly visible. A few isolated peaks are also present in the MK spectrum (around 19 and 25.5°), which could be attributed to traces of muscovite, illite, or even kaolinite. In SF, the main feature of the XRD spectrum is a wide bump between 15 and 35° , typical of a significant amorphous content; no obvious crystalline phase is identified, despite

the presence of a couple of peaks (at 36 and 60°). The main crystalline features of MK and SF are also present in reference GP before fire test, and in all formulations before and after fire test. The presence of cristobalite (heat-transformed structure of SiO₂) is also noted with a small main peak at 22°. As expected, it is concluded that no accurate structural characterization of GP is possible by XRD.

NMR results.

The analysis below uses the general structure of hardened GP polymeric network proposed in [70-71].

Before and after fire test, the ²³Na MAS NMR spectra of the GP coatings are presented in Figure 4(a). A narrow resonance is observed at approximately 0 ppm within the spectra of reference GP before fire testing. It is attributed to sodium cations, which provide a charge balancing function for Al(OH)₄. In other words, Na⁺ is in a hydrated state [72] in the cavities of the geopolymer. Na⁺ is also present in a less hydrated state, as a compensating cation, playing a role in the formation of the polymeric network, as suggested in the literature [70-71]. After fire test, the spectra of the three samples, reference GP and GP foam n.1 and n.2 exhibit a single broad resonance centered at approximately -11 ppm. It is attributed to sodium associated with aluminium-centered tetrahedra, in a charge balancing capacity within the alkali aluminosilicate framework [73].

For all GP coatings, ²⁷Al MAS NMR spectra (Figure 4(b)) show a broad band centered at 55 ppm, which is assigned to aluminum in tetrahedral site (Al^{IV}). The presence of a broad Al^{IV} band in all materials is consistent with well-formed geopolymers [74]. It is also noteworthy that the Al^{IV} band is significantly broadened after fire test, because the GP structure becomes more disordered.

A broad band of low intensity can also be distinguished at 30 ppm especially in the spectrum of reference GP before fire test. This broad band is assigned to five-coordinated aluminum sites (Al^V). Single or double bands located at 10 and 5 ppm are observed on all spectra. They are assigned to octahedral sites (Al^{VI}) [75]. Both (Al^V) and (Al^{VI}) are generally attributed to mullite-like environments [76]. In our case, they are attributed to non-reacted SF and MK, i.e. SF and MK not consumed during the geopolymerization process.

Regarding the ^{29}Si NMR spectra (Figure 5), the chemical shifts of GP lie between -125 and -75 ppm. All spectra exhibit broad bands. These broad resonances are the signatures of a distributed and disordered structure. Before fire test, the spectra exhibit a higher resolution and four narrow resonances can be clearly distinguished from the overall broad contribution. These noticeable bands are centered at -80, -88, -97 and -107 ppm and show the presence of crystalline compounds in the materials, in addition to the amorphous phases highlighted by the broad NMR signals.

The spectra are decomposed using mixed Gaussian-Lorentzian bands to get more information about the species formed during the polymerization (Figure 5, dotted lines). Six or seven bands are used, considering that $Q^4(mAl)$ and Q^4 sites should be formed (see Appendix 1). $Q^4(4Al)$, $Q^4(3Al)$, $Q^4(2Al)$ and $Q^4(1Al)$ sites are located at -80, -88, -93, -98 ppm respectively [49,73]. These sites characterize the formation of the geopolymer. Note that GP foam n.1 does not form $Q^4(4Al)$. This might mean that the presence of hydrogen peroxide promotes a less polymerized structure of GP foam n.1, but this is not observed with GP foam n.2, possibly owing to CTABr. The band at -103 ppm is assigned to Q^4 site in unreacted MK [70-71]. It is consistent with the assignment done by ^{27}Al NMR. The sharp band at -107 ppm is assigned to Q^4 site in quartz [77]; it is consistent with XRD characterization (see Appendix 1). The band

at -110 ppm is assigned to Q^4 site in silica fume (SF) [78], which is used in the formulation of all GP coatings.

The decomposition allows to quantify the nature of the silicate species. The area under each mixed Gaussian-Lorentzian band is calculated, and the proportion of each Q^n site is derived as the ratio between the areas under the mixed Gaussian-Lorentzian bands and their sum. Table 3 summarizes the main quantitative results.

Before fire test, 60 and 68% of the total amount of silicon atoms of the 3 coatings contribute to GP alumino-silicates (these are calculated as the sum of $Q^4(4Al)$, $Q^4(3Al)$, $Q^4(2Al)$ and $Q^4(1Al)$ site proportions only). After fire test, the narrower bands are no longer observed, and the lineshape of the bands is poorly defined. It suggests the presence of an amorphous structure. The three spectra after fire test are also decomposed. The same species (as commented above), corresponding to a distribution of $Q^4(4Al)$, $Q^4(3Al)$, $Q^4(2Al)$ and $Q^4(1Al)$ sites and Q^4 sites, are found. The decomposition suggests that 53- 58% of the total amount of silica is found as alumino-silicates in the coatings whatever the formulation. Therefore, the effect of the flame does not consist in creating new species. It rather makes the GP structure more amorphous. The geopolymers also depolymerize, with a decrease by 10% in the amount of aluminosilicates, mainly *via* a decrease in the amounts of $Q^4(3Al)$ and $Q^4(2Al)$ sites (by about 8%), to yield similar Si environments as in silica fume and metakaolin.

3.2.2.- Pore structure

Macrophotographs. A visual inspection of reference GP and GP foams n.1 and n.2 is performed after 7 days curing and before or after fire test (Figure 6).

Before fire test, small open bubbles are present at the surface of reference GP. They are attributed to the reaction of silicon with the water present in the GP, which creates dihydrogen

gas (according to: $4 \text{ H}_2\text{O} + \text{Si} \rightarrow 2 \text{ H}_2 + \text{Si(OH)}_4$ [10]). Dihydrogen is released as small bubbles in the coating during the setting of GP cement.

Comparatively, GP foam n.1 comprises a number of open bubbles, significantly bigger in size than reference GP. These bubbles are attributed to oxygen gas, obtained through the reaction of hydrogen peroxide in the GP (according to $\text{H}_2\text{O}_2 \rightarrow \frac{1}{2} \text{ O}_2 + \text{H}_2\text{O}$ [29]). Upon formation, oxygen gas bubbles reach the coating surface and a number of them does not remain inside the GP solids. Further, GP foam n.2 does not present such big open bubbles on its surface, very probably owing to the stabilizing effect of CTABr. However, due to the quantity of CTABr involved in its formulation, GP foam n.2 is less fluid than the other GP coatings. It has proven more difficult to apply on the steel plate, as also shows its general aspect (Figure 6).

Moreover, all foams are cured for 7 days in a hermetic bag, i.e. without any particular precaution against atmospheric CO_2 – the only precaution is against water removal. Despite this, no efflorescence, attributable to carbonation, is observed at the surface of the foams. Although carbonation may affect the samples on longer durations (in particular after 28 days curing) [22], these foams do not seem actually sensitive to CO_2 presence.

After fire, a network of micro-cracks is observed on all three GP coatings, but, remarkably, their general structure is preserved. In particular, none of the three GP coatings has detached from the steel plate. This is attributed to a good adhesion of GP on the sandblasted steel plate. Visual inspection of the coatings along their thickness shows different pore structures. The latter are analyzed in a qualitative manner by electron probe micro-analysis and quantitatively by X ray micro-CT, as follows.

Electron probe micro-analysis. Figure 7 shows the chemical mapping for Si, Al and Na for GP foam n.1 before and after fire test. The mapping evidences that the initially plain silica

fume particles are expanded, i.e. they comprise significant amounts of inner voids. These voids are due to the intense heat of the fire test. Similar results are obtained with reference GP and GP foam n.2 (not shown).

X ray micro-CT results.

Figure 8 shows typical grey level images of the three GP coatings, before and after fire test. The analysis is completed by the quantitative analysis of the pore structure (Table 4 and Figure 9).

In Figure 8, pores are in black and the GP solids are in various grey values. Silica fume grains appear in darker grey; they are clearly highly porous after fire, as evidenced with electron probe micro-analysis (see above). MK particles are in the lightest grey value.

Before fire test, for reference GP (without foaming agent except silica fume) and GP foam n.1 (added with H₂O₂ only), a similar pore structure of isolated bubbles, dominated by the GP solids, is observed. For GP foam n.2 (added with H₂O₂ and foam stabilizer CTABr), a different pore structure is obtained, which is of cellular-type, dominated by voids separated by thin GP cement walls. After fire test, the main common feature for all three GP coatings is the significant expansion of silica fume particles, which generates a significant amount of pores smaller than the initial foam pores.

This observation is confirmed by quantitative pore analysis (Table 4 and Figure 9). Indeed, after fire, whatever the GP coating considered, Figure 9 clearly shows an increase in smaller pore sizes, well below 1 mm diameter. Data analysis of the expanded silica fume particles alone, as observed in Figures 7 and 8, shows that their typical pore size ranges precisely between 13 microns and 1 mm.

Before fire test, Fig. 9 also highlights the difference in pore structure of the three GP coatings. Pore size distributions (PSD) have a similar range from 0.012-1.9 mm for reference GP and 0.012-1.3 mm for foam n.1, with a d_{50} significantly smaller than 1 mm, at respective values of 0.49 mm and 0.60 mm (Table 4). On the opposite, the PSD of GP foam n.2 is more widely distributed, with sizes spanning almost the whole investigated range (12 microns to 3.4 mm), and a d_{50} of 3.0 mm. Moreover, 80% of the pores of GP foam n.2 are bigger than 2.7 mm. This is associated with the particular cellular pore structure of GP foam n.2.

Further, Table 4 provides the porosity (i.e. the relative pore volume) of the GP coatings before and after fire. It is noted that before fire, porosity is only slightly increased when comparing reference GP and GP foam n.1 (with values of 24.5 and 30.0% respectively), meaning that H_2O_2 alone does not change significantly the GP pore structure. With both H_2O_2 and CTABr (GP foam n.2) however, a significantly bigger porosity is obtained (at a value of 81.0%), when compared to reference GP.

For all three formulations, d_{50} is smaller after the fire test than before (Table 4). This is attributed to the expansion of the silica fume particles, which creates smaller pores inside the coatings. For reference GP and GP foam n.1, this contributes to an increase in porosity and a decrease in d_{50} .

For GP foam n.2, the effect of silica fume is slightly different. The cellular structure is marked by a few breakages of GP cement walls, and by silica fume expansion. After fire, the PSD has a significantly greater number of pores smaller than 3 mm than before fire. However, this does not affect the overall pore structure; for this foam, d_{50} and porosity remain almost unchanged.

2.2.3. Thermal conductivity

The heat conductivity of the GP coatings is presented in Figure 10, before and after fire testing. As expected, all conductivities lie between 0.075 and 0.3 W/(m.K), indicating that all materials are low thermal conductors. Moreover, those values are consistent with data reported by Jaya et al. [79] on similar GPs and GP foams.

Analysis of the heat transfer mechanisms. When the geopolymer undergoes fire exposure, it creates a heat gradient inside the material from roughly 600°C on the front side up to 400°C the backside in the stationary state. Those temperature changes can modify the internal structure of the geopolymers and hence, their thermal conductivity.

The thermal conductivity of reference bulk GP increases only slightly after the fire test. As described above, due to the fire, SF expands upon fire. Smaller pores (than the original ones) are created, which contributes to decrease thermal conductivity; simultaneously, porosity increases, which also contributes to decrease thermal conductivity. However, sample cracking due to fire test contributes to open the pores and increases thermal conductivity. These antagonistic effects explain the stability in the heat conductivity of reference GP.

Before fire testing, GP foam n.1 has a slightly higher heat conductivity than that of reference GP, in good agreement with a higher porosity. However, this value is highly variable (Figure 10), due to a significant inhomogeneity of the foam at the centimetric scale. After fire testing, mainly due to SF expansion, porosity of GP foam n.1 increases and it gains smaller pores, so that both effects contribute to decrease significantly its heat conductivity, from 0.3 W/mK to 0.14 W/mK (i.e. by a factor of 2.1). The presence of cracks (observed after fire testing) does not appear to affect thermal conductivity significantly.

For GP foam n.2, porosity is hardly affected by the fire test, but SF provides small pores after fire, which contributes to decrease its thermal conductivity, from 0.18 W/mK to 0.09 W/mK

(i.e. by a factor of 2). As for GP foam n.1, the presence of cracks (created by fire testing) does not appear to affect thermal conductivity significantly.

The heat conductivities of the three GP coatings, and their differences, are also indicative of their fire performance (Figure 2b). GP foam n.2 has the lowest heat conductivity before and after testing and hence, its temperature rise is the slowest. Its relatively low temperature in the steady state is governed by the low heat conductivity measured after fire test. In the case of GP foam n.1, the temperature rise is slower than for reference GP, while the two coatings have similar heat conductivity before fire testing (although it is slightly bigger for GP foam n.1).

During temperature rise, the time-temperature curve is not formally governed by heat conductivity, but by thermal diffusivity ($\alpha = \frac{k}{\rho \cdot c_p}$) where α is thermal diffusivity, k heat conductivity, ρ volumetric mass and c_p heat capacity. These three parameters (k , ρ and c_p) depend on temperature, so that there is a direct proportionality between thermal diffusivity α and heat conductivity k .

According to porosities given in Table 4, and given that the coatings are deposited at constant mass, it is assumed that the volumetric mass of GP foam 1 is greater than that of reference GP. By also assuming similar values for c_p because of similar chemical composition, the thermal diffusivity of GP foam 1 should be lower than for reference GP. A lower thermal diffusivity explains why the temperature rise of GP foam 1 is lower than that of reference GP. In the steady state, the temperature is governed by heat conductivity and hence, the temperature in the case of GP foam 1 is lower than that of reference GP.

Another driving factor explaining the kinetics of temperature rise during the burn through test is the coating thickness; the thicker the coating, the slower the temperature rise. For reference GP, the thickness is 3.2 mm +/-0.3; for GP foam n.1 it is 5.5 mm +/-0.3 and for GP foam n.2

it is 10.7mm +/- 4.4 (Table 2). Therefore, the temperature rise evolves exactly inversely as the coating thickness.

4- Discussion and analysis: understanding the thermal conductivity of GP foams

4.1- Available modelling approaches

Geopolymers are heterogenous materials which can be considered as porous materials constituted by a solid skeleton (geopolymer) and a fluid (air). The thermal conduction in such materials is a complex process involving different types of heat mechanism depending on their structure, pore size distribution, chemical composition and so forth.

Analytical models have been developed to calculate the effective heat conductivity of heterogenous materials including the structure and the type of porosity of the material. Five basic structural models can be found in the literature: the Series [80], Parallel [80], Maxwell–Eucken [81] (two forms) and Effective Medium Theory (EMT) [82] models. They are described in detail in Appendix 2.

4.2- Application to GP foams

The geopolymers in this study are constituted of a solid aluminosilicate skeleton and of distributed pores of different sizes.

To apply the structural models commented above, it is necessary to assume a mean heat conductivity of the solid k_s , and a mean heat conductivity of the fluid k_f [84]. In this research, the fluid considered is the air ($k_f = 0.026$ W/m.K at room temperature), and k_s of the solid is extrapolated using data from the literature. Xu et al. [85] prepared geopolymer foams with similar composition to our materials, and they measured the thermal conductivity as a function of porosity. By extrapolating their data at 0 porosity, a value of k_s is estimated at

0.85 W/(m.K). Porosity was determined previously, so that the effective thermal conductivity (k_e) can be calculated for the six structural models and compared to the experimental values. All the values are gathered in Table 6 to make the comparison between experimental and calculated data easier. It is noteworthy that k_m is used as an adjusting parameter, but its physical meaning is discussed in relation with the structure of the geopolymers in the following.

When discussing heat conductivity, the terms ‘continuous phase’ and ‘dispersed phase’ can be ambiguous because these are defined in relation to optimal heat transfer pathways, to distinguish between the dispersed phase (not optimal for heat transfer) and the continuous phase (optimal for heat transfer), and not from the actual material solid/fluid components. For instance, a granular/particulate medium is a heap of solid grains with limited heat transfer ability; the solid grains may be considered as the dispersed phase comparatively to the actual material voids (forming a continuous phase for heat transfer).

In this context, Figure 11 plots relative heat conductivities (k_e/k_s) predicted by the Series, Parallel, Maxwell-Eucken 1 and 2 and EMT models for the three formulations, before and after fire testing. Complementarily to continuous or dispersed phases in a porous medium, according to Carson et al. [86], porous materials are divided into two classes from the heat transfer viewpoint, corresponding to two zones in the diagram: (1) ‘internal porosity’ materials, which have bubbles (i.e. a dispersed phase) suspended within a continuous condensed phase and (2) ‘external porosity’ materials with (generally) smaller void proportions, but including granular/particulate materials as the dispersed phase. In both cases, the dispersed phase has the worst heat transfer ability.

In Fig.11, it is observed that reference GP and GP foam 1 (before and after fire testing) belong to the category of external porosity materials, where the continuous phase is the air

contained in the material. As seen in micro-CT analysis (Figs. 8 and 9, Table 4), the gaseous phase occupies 24.5 to 30% of the total space, i.e. less than the solids, but the calculation indicates that the fluid behaves as a continuous phase from a heat transfer perspective. This means that the air voids in the material form a percolating phase with better heat transfer ability than the solids. Indeed, the heat transfer pathways are strongly dependent on the quality of the thermal contact between the particles, and this suggests that a limited heat transfer occurs in the solid skeleton of geopolymers and makes it the ‘dispersed’ phase (for heat transfer alone).

On the contrary, GP foam 2 exhibits a pure parallel behavior before testing and behaves as an ‘internal porosity’ material after fire testing. The parallel model suggests that the components are aligned parallel to the heat flow. For an ‘internal porosity’ material, the majority of the heat flow is through the condensed phase. In GP Foam 2 after fire, the porosity is quite high. It makes sense that heat transfer is governed by the solid phase, with in that case $k_f \ll k_s$.

4.3- Comparison between modelling and experiments

The comparison of the calculated thermal conductivity with the experimental values shows that no structural model can describe the effective thermal conductivity of the geopolymers (except for GP foam 2 before fire testing).

However, the introduction of the 6th structural model (NEMT) provides good agreement with the experimental values, thanks to an additional parameter k_m . This parameter is the thermal conductivity of an assumed uniform medium in which all the components (phases) are dispersed. All the assumptions of this model are detailed and commented in [87]. GP foam 2 before fire testing takes a particular value of k_m ($k_m = 15 \text{ W/(m.K)} \gg k_f$ and k_s , and after simplification, the NEMT equation becomes the parallel equation, which leads to the parallel model. High values of k_m were observed in fibrous materials [83], and it suggests that in

terms of heat transfer, GP foam 2 may exhibit a strong anisotropy. For the other geopolymers, k_m lies between 0.04 and 0.17 W/(m.K). Low values of k_m ($k_m < 0.1$ W/(m.K)) are characteristic of materials exhibiting heat conduction similar to dry sand [81]. This is the case of reference GP and GP foam 1, suggesting that the structure formed favors heat transfer via the gaseous phase.

5- Conclusions

This experimental research characterizes two novel GP foam coatings based on alkali-activated MK, SF and hydrogen peroxide (stabilized -or not- by a CTABr surfactant). These coatings provide an excellent thermal barrier for steel against burn-through fire. At the back of a steel plate, the temperature is decreased by 251°C with GP foam n.2 (made with H₂O₂ and CTABr), whereas it is decreased by 122°C with bulk GP and by 203°C with GP foam n.1 (with H₂O₂ only). The thermal barrier effect is improved by CTABr, which increases the foam thickness from 5.5 mm (GP foam n.1) to 10.7 mm (GP foam n.2).

In the coatings, the GP cement structure is mainly amorphous. Solid state MAS NMR of ²³Na, ²⁷Al and ²⁹Si clearly shows that after fire, the solids retain a significant part of their chemical integrity.

Quantitative X ray micro-CT shows that after fire, SF expands and creates smaller pores (than those existing before fire) in the GP. For GP foam n.2, with a cellular structure, porosity remains stable, and pore sizes decrease, inducing a more limited decrease of thermal conductivity than with GP foam n.1.

Fitting usual thermal conductivity models to the experimental data shows that for reference GP and GP foam 1, heat transfer takes place mainly through the air voids, meaning that the GP solids are limited heat conductors (similar to sand grains). For the cellular structure of GP foam 2, heat transfers preferentially through the solids than through the 81% porosity, providing the best heat insulation properties.

In this research, all GP coatings are cured for only 7 days. In practice, serious fires in steel structures have a low probability, and even more so at 7 days after being coated with GP foams. Therefore, the long-term stability and fire resistance of the proposed GP foams will be investigated in further investigations.

Acknowledgements

This work has received funding from the European Research Council (ERC) under the European Union's H2020- the framework programme for Research and Innovation (2014-2020) ERC Grant Advances Agreement N°670,747-ERC 2014 AdG/FireBar-Concept for FireBar Concept project. The authors are grateful to Benjamin Dewailly for technical assistance, to Séverine Bellayer for EPMA analysis, to Leo Amichot for preliminary tests, and to LilloA (Lille Open Archive) for making the preprint of this article available as an open access document.

The ISIS4D X-Ray CT platform has been funded by International Campus on Safety and Intermodality in Transportation (CISIT), the Hauts-de-France Region, the European Community and the National Center for Scientific Research. The authors gratefully acknowledge the support of these institutions. The SEM and electron probe facilities in Lille (France) are supported by the Conseil Régional du Nord-Pas de Calais (France), and the European Regional Development Fund (ERDF). Chevreul Institute (FR 2638), Ministère de l'Enseignement Supérieur et de la Recherche, Région Hauts de France, and FEDER are acknowledged for supporting and funding XRD facilities.

Appendix 1: Characterization methods

1- ²⁹Si and ²⁷Al MAS NMR: spectra acquisition and analysis

Acquisition method. The ²⁹Si MAS NMR experiments are acquired at 79.5 MHz on a 9.4 T Bruker spectrometer. The experiments are done at a spinning frequency (ν_{rot}) of 5 kHz on a 7-mm probehead with a pulse length of 5 μs ($\pi/2$ flip angle), 80 transients and a recycle delay (rd) of 180-300 s. The ²³Na and ²⁷Al NMR spectra are acquired at 211.6 and 208.5 MHz, respectively, on a 18.8 T Bruker spectrometer using a 3.2-mm probehead operating at a ν_{rot} of 20-22 kHz. The ²³Na NMR spectra are obtained with a pulse length of 1 μs ($\sim\pi/5$ flip angle), 128-256 transients, and a recycle delay of 1 s. The ²⁷Al NMR spectra are recorded with a pulse length of 1 μs ($\sim\pi/8$ flip angle), 256 transients, and a recycle delay of 0.5-1 s. The ²⁹Si, ²³Na and ²⁷Al NMR spectra are referred to liquid TMS, NaCl (1 M) and Al(NO₃)₃ (1 M), respectively, as 0 ppm.

Data analysis. Following data acquisition, the chemical shift of silicon is determined by the chemical nature of its neighbors, namely, the number of siloxane bridges attached to a silicon atom. M, D, T and Q structures form the commonly used notation corresponding to one, two, three and four Si–O– bridges, respectively. According to the chemical composition of the prepared geopolymer, Si can only be in a Q structure. The Qⁿ notation corresponds to Si(OR')₄, where n denotes the number of bridging oxygens surrounding the silicon atom [88]. Geopolymers are polysialates and hence, they involve Al–O–Si bonds. The notation Qⁿ(mAl) is then commonly used for characterizing the aluminosilicates, where $0 \leq m \leq n \leq 4$. n is the coordination number of the silicon center, and m is the number of Al neighbors, used to describe the connectivity of a silicon tetrahedron bridged through oxygen to aluminum and to other silicon centers [89]. According to Walkley et al. [73], the usual coordination number n in GP is 4. Lower coordination Si species ($0 \leq n \leq 3$) are not commonly observed.

2- X Ray Diffractometry (XRD)

Experimental procedure. After 7 days curing, before and after fire test, the GP samples are characterized qualitatively by X ray diffraction. MK and silica fume are also tested as reference materials. Prior to the analysis, each material is ground in a powder form and tested in a BRUKER© D8 advance (Cu K α radiation) apparatus, with a 2θ angle between 5° and 80°, at a step of 0.02°, with an analysis time of 0.5 seconds.

3- Electron probe micro-analysis

All GP samples (three formulations before and after fire) are coated in epoxy resin and polished until mirror finish using abrasive disks. BSE imaging is performed with a Scanning Electron Microscope (JEOL JSM 7800F LV, JEOL ltd, Tokyo, Japan) operated at 15 kV. Cross-section X-ray mappings are carried out at an acceleration voltage of 15 KV, 40 nA using a Camera SX100 electron probe microanalyser (Electron Probe Micro-Analysis: EPMA) (Cameca, Gennevilliers, France). On the mappings, a color-coded legend characterizes the concentration of the element (black color: absence of the element to red color: highest concentration).

4- X ray micro-Computed Tomography (micro-CT)

The apparatus is equipped with a nano focus tube operated at a 60kV tension and 35uA current, with a flat detector panel of 1874x1496 pixels². Each image series (1440 images over 15min in total, with an averaging of 6 images per angular position) corresponds to one different sample of GP foam (reference, foam n.1 and foam n.2) after 7 days curing, and observed before or after fire test, see Table 3. After the reconstruction procedure (along the Z axis, with a filtered retro-projection algorithm) and acquisition artifacts removal, an output volume is computed, composed of 924-1063 images in a (X, Y) plane (at 1.39-2.40 x 10⁶ pixels² each) regularly spaced from one another by 6.75 microns. The corresponding cubic

voxel size is of 307.5 micron^3 . Each sample corresponds to huge datasets of $1.48\text{-}2.55 \times 10^9$ voxels³, linearly scaled into a 16-bit format.

Appendix 2: description of heat conductivity models for heterogenous materials

Analytical models have been developed to calculate the effective heat conductivity of heterogenous materials including the structure and the type of porosity of the material. Five basic structural models are found in the literature: the Series [80], Parallel [80], Maxwell–Eucken [81] (two forms) and Effective Medium Theory (EMT) [82] models.

In all these models, the material is assumed made of two components; one component is the fluid and the other the solid. The physical structures assumed in the derivations of the Series and Parallel models are of layers of the components aligned either perpendicular or parallel to the heat flow. In the parallel model, there is no heat transfer between the solid skeleton and the fluid because heat transfers in solid and fluid occur at the same time. In the series model, heat transfer occurs between the solid and the fluid in perpendicular direction to the pore channel.

The Maxwell–Eucken model assumes a dispersion of small spheres within a continuous matrix of different components, with the spheres being far enough apart such that the local distortions to the temperature distribution around each of the spheres do not interfere with their neighbor temperature distributions. For the two-component material, two forms of the Maxwell–Eucken model arise depending on which of the components creates the continuous phase. The model considers that the pores are dispersive and not connected: (i) in Form 1, the solid component is continuous and (ii) in Form 2, the pores are the continuous phase.

The EMT model assumes a completely random distribution of all components. A novel revised EMT model has been reported by Gong et al [83], which unifies the five basic structural models. The components are treated as small spheres dispersed into an assumed uniform medium with thermal conductivity k_m (i.e. heat conduction from the solid to the

fluid). When this last parameter takes a particular value, all 5 models can be retrieved. Table 5 gathers the two-component forms of the equations for each of these models, along with a schematic of its assumed physical structure.

References

- [1] J. Wang, G. Wang, Influences of montmorillonite on fire protection, water and corrosion resistance of waterborne intumescent fire retardant coating for steel structure, *Surf. Coat. Technol.* 239 (2014) 177–184.
- [2] M. Lahoti, K. H. Tan, E. H. Yang, A critical review of geopolymer properties for structural fire-resistance applications, *Constr. Build. Mater.*, 221 (2019) 514–526.
- [3] X. Peng, H. Li, Q. Shuai, L. Wang, Fire Resistance of Alkali Activated Geopolymer Foams Produced from Metakaolin and Na_2O_2 , *Materials*, 13 (2020) 535-542.
- [4] J. Alongi, Z. Han, S. Bourbigot, Intumescence: Tradition versus novelty. A comprehensive review, *Prog. Polym. Sci.* 51 (2015) 28-73.
- [5] M. B. Wong, Temperature analysis of partially heated steel members in fire, *Journal of Constructional Steel Research*, 128 (2017) 1–6.
- [6] L. Carabba, R. Moricone, G. E. Scarponi, A. Tugnoli, M. C. Bignozzi, Alkali activated lightweight mortars for passive fire protection: A preliminary study, *Constr. Build. Mater.*, 195 (2019) 75-84.
- [7] R. E. Lyon, P. N. Balaguru, A. Foden, U. Sorathia, J. Davidovits, M. Davidovics, Fire-resistant Aluminosilicate Composites, *Fire Mater.*, 21 (1997) 67-73
- [8] J. A. Hammell, P. N. Balaguru, R. E. Lyon. Strength retention of fire resistant aluminosilicate-carbon composites under wet-dry conditions. *Compos. Part B*, 31 (2000) 107–111.
- [9] J. L. Bell, W. M. Kriven, Preparation of ceramic foams from metakaolin-based geopolymer gels, in *Development in Strategic Materials*, Ed. H.-T. Lin, K. Koumoto, W. M. Kriven, E. Garcia, I. E. Reimanis, D. P. Norton, The American Ceramic Society, (2009) 97-111

- [10] M. B. Watolla, G. J. G. Gluth, P. Sturm, W. D. A. Rickard, S. Krüger, B. Scharrel, Intumescent Geopolymer-Bound Coatings for Fire Protection of Steel, *J. Ceram. Sci. Technol.*, 08 (3) (2017) 351-364
- [11] Y. C. Wang, J. P. Zhao, Facile preparation of slag or fly ash geopolymer composite coatings with flame resistance, *Constr. Build. Mater.*, 203 (2019) 655-661
- [12] J. Davidovits, 'Geopolymers', *J Therm Anal.* 37(8) (1991) 1633-1656
- [13] J. Davidovits, 30 Years of Successes and Failures in Geopolymer Applications. Market Trends and Potential Breakthroughs, Geopolymer 2002 Conference, 2002, Melbourne, Australia
- [14] M. Hussain, R. J. Varley, Y. B. Cheng, G. P. Simon. Investigation of thermal and fire performance of novel hybrid geopolymer composites, *J Mater Sci* 39 (2004) 4721–6
- [15] G. Kovalchuk, P. V. Krivenko. Producing fire- and heat-resistant geopolymers. In: Provis JL, van Deventer JSJ, editors. *Geopolymers: structures, processing, properties and industrial applications*. Cambridge, UK: Woodhead, (2009) 227–63
- [16] J. L. Provis, J. S. J. van Deventer, editors. *Geopolymers: structures, processing, properties and industrial applications*. Abingdon, UK: Woodhead Publishing, 2009
- [17] J. Davidovits, *Geopolymer Chemistry and Applications*, Geopolymer Institute, Saint-Quentin, France, 2011
- [18] G. Masi, W. D. A. Rickard, M. C. Bignozzi, . van Riessen, The effect of organic and inorganic fibres on the mechanical and thermal properties of aluminate activated geopolymers, *Compos. Part B*, 76 (2015) 218-228.
- [19] F. Colangelo, R. Cioffi, G. Roviello, I. Capasso, D. Caputo, P. Aprea, B. Liguori, C. Ferone, Thermal cycling stability of fly ash based geopolymer mortars, *Compos. Part B*, 129 (2017) 11-17.

- [20] A. Hajimohammadi, T. Ngo, J. L. Provis, T. Kim, J. Vongsvivut, High strength/density ratio in a syntactic foam made from one-part mix geopolymer and cenospheres, *Compos. Part B*, 173 (2019) 106908.
- [21] M. A. Longhi, B. Walkley, E. D. Rodriguez, A. P. Kirchheim, Z. Zhang, H. Wang, New selective dissolution process to quantify reaction extent and product stability in metakaolin-based geopolymers, *Compos. Part B*, 176 (2019) 107172.
- [22] M. A. Longhi, E.D. Rodriguez, B. Walkley, Z. Zhang, A. P. Kirchheim, Metakaolin-based geopolymers: Relation between formulation, physicochemical properties and efflorescence formation, *Compos. Part B*, 182 (2020) 107671
- [23] N. Li, C. Shi, Z. Zhang, H. Wang, Y. Liu, A review on mixture design methods for geopolymer concrete, *Compos. Part B*, 178 (2019) 107490
- [24] M. A. Longhi, B. Walkley, E. D. Rodriguez, A. P. Kirchheim, Z. Zhang, H. Wang, New selective dissolution process to quantify reaction extent and product stability in metakaolin-based geopolymers, *Compos. Part B*, 176 (2019) 107172
- [25] C. Bai, A. Conte, P. Colombo, Open-cell phosphate-based geopolymer foams by frothing, *Mater. Lett.* 188 (2017) 379–382
- [26] C. Bai, G. Franchin, H. Elsayed, A. Zaggia, L. Conte, H. Li, High-porosity geopolymer foams with tailored porosity for thermal insulation and wastewater treatment, *J. Mater. Res.*, 32(17) (2017) 3251–3259
- [27] C. Bai, P. Colombo, High-porosity geopolymer membrane supports by peroxide route with the addition of egg white as surfactant, *Ceram. Int.* 43 (2017) 2267–2273
- [28] C. Bai, H. Li, E. Bernardo, P. Colombo, Waste-to-resource preparation of glass-containing foams from geopolymers, *Ceram. Int.* 45 (2019) 7196–7202
- [29] S. Petlitckaia, A. Poulesquen, Design of lightweight metakaolin based geopolymer foamed with hydrogen peroxide, *Ceram Int*, 45(1) (2019) 1322–1330

- [30] Q. Shuai, Z. Xu, Z. Yao, X. Chen, Z. Jiang, X. Peng, Fire resistance of phosphoric acid-based geopolymer foams fabricated from metakaolin and hydrogen peroxide, *Mater. Lett.* 263 (2020) 127228-127232
- [31] H. Celerier, J. Jouin, N. Tessier-Doyen, S. Rossignol, Influence of various metakaolin raw materials on the water and fire resistance of geopolymers prepared in phosphoric acid, *J. Non-Cryst. Solids*, 500 (2018) 493–501
- [32] P.V. Krivenko, Y. K. Pushkavera, M. V. Sukhanevich, S. G. Guziy, Fireproof coatings on the basis of alkaline aluminum silicate systems, *Ceram. Eng. Sci. Proc.*, 29(10) (2009) 129 – 142
- [33] P. Duxson, G. C. Lukey, J. S. J. van Deventer, *J. Non-Cryst. Solids*, 352 (2006) 5541–5555
- [34] P. Duxson, G. C. Lukey, J. S. J. van Deventer, Thermal evolution of metakaolin geopolymers: Part 2 - Phase stability and structural development, *J. Non-Cryst. Solids*, 353 (2007) 2186-2200
- [35] P. Duxson, G. C. Lukey, J. S. J. van Deventer. Physical evolution of Na-geopolymer derived from metakaolin up to 1000°C. *J Mater Sci* 42 (2007) 3044–54
- [36] S. A. Bernal, E. D. Rodriguez, R. M. De Gutierrez, M. Gordillo, J. L. Provis, Mechanical and thermal characterization of geopolymers based on silicate-activated metakaolin/slag blends, *J Mater Sci*, 46 (2011) 5477-5486
- [37] S. A. Bernal, J. Bejarano, C. Garzon, R. M. De Gutierrez, S. Delvasto, E.D. Rodriguez, *Compos. Part B*, 43 (2012) 1919-1928
- [38] M. Lahoti, K. K. Wong, E. H. Yang, K. H. Tan, Effects of Si/Al molar ratio on strength endurance and volume stability of metakaolin geopolymers subject to elevated temperature, *Ceram Int* 44 (2018) 5726-5734

- [39] V. F. F. Barbosa, K. J. D. MacKenzie, Thermal behavior of inorganic geopolymers and composites derived from sodium polysialate, *Mat Res Bulletin*, 38 (2003) 319-331
- [40] J. L. Bell, P. E. Driemeyer, W. M. Kriven, Formation of Ceramics from Metakaolin-Based Geopolymers. Part II: K-Based Geopolymer, *J. Am. Ceram. Soc.*, 92(3) (2009) 607–615
- [41] T. Bakharev, Thermal behaviour of geopolymers prepared using class F fly ash and elevated temperature curing, *Cem. Concr. Res.*, 36 (2006) 1134–1147
- [42] Y. L. Galiano, C. Leiva, C. Arenas, F. Arroyo, L. Vilches, C. Fernandez-Pereira, *Waste Biomass Valorization*, 8 (2017) 2485-2494
- [43] C. Leiva, Y. Luna-Galiano, C. Arenas, B. Alonso-Farinas, C. Fernandez-Pereira, A porous geopolymer based on aluminum-waste with acoustic properties, *J. Waste Manage.*, 95 (2019) 504–512
- [44] A. M. Rashad, Insulating and fire-resistant behaviour of metakaolin and fly ash geopolymer mortars, *Proceedings of the Institution of Civil Engineers-Construction Materials*, 172(1) (2019) 37-44
- [45] R. J. Myers, B. Lothenbach, S. A. Bernal, J. L. Provis, Thermodynamic modelling of alkali-activated slag cements, *Appl. Geochem.*, 61 (2015) 233–247
- [46] T. Yang, H. Zhu, Z. Zhang, Influence of fly ash on the pore structure and shrinkage characteristics of metakaolin-based geopolymer pastes and mortars, *Constr. Build. Mater.*, 153 (2017) 284–293
- [47] A. Nmiri, M. Duc, N. Hamdi, Replacement of alkali silicate solution with silica fume in metakaolin-based geopolymers, *Int J of Minerals Metallurgy and Materials*, 26(5) (2019) 555-564.

- [48] M. Sarkar, K. Dana, S. Das, Microstructural and phase evolution in metakaolin geopolymers with different activators and added aluminosilicate fillers, *J. Mol. Struct.*, 1098 (2015) 110-118
- [49] P. Duxson, J. L. Provis, G. C. Lukey, S. W. Mallicoat, W. M. Kriven, J. S. J. van Deventer, Understanding the relationship between geopolymer composition, microstructure and mechanical properties, *Colloids Surf. Physicochem. Eng. Asp.*, 269(1) (2005) 47-58
- [50] M. A. Villaquiran-Cacedo, R. Mejia de Gutierrez, *J Am Ceram Soc.* 102 (2019) 3653–3662
- [51] T. Cheng, J. Chiu, Fire-resistant geopolymer produced by granulated blast furnace slag, *Miner Eng.* 16 (2003) 205-10
- [52] V. C. Li, M. Maalej, Toughening in cement based composites. Part I. Cement, mortar and concrete, *Cem Concr Compos* 18 (1996) 223–37
- [53] W. N. U. Van Bonin, U. Von Gizycki, Hydrogen peroxides blowing agent for silicate foams, US Patent 3,864,137, 1975
- [54] V. Vaou, D. Parias, Thermal insulating foamy geopolymer from perlite, *Miner Eng* 23 (2010) 1146–51
- [55] A. Hajimohammadi, T. Ngo, P. Mendis, T. Nguyen, A. Kashani, J.S. J. van Deventer, Pore characteristics in one-part mix geopolymers foamed by H₂O₂: The impact of mix design, *Mater. Des.*, 130 (2017) 381–391
- [56] E. Prud'homme, P. Michaud, E. Joussein, C. Peyratout, A. Smith, S. Arrii-Clacens, Silica fume as porogent agent in geo-materials at low temperature, *J. Eur. Ceram. Soc.*, 30 (2010) 1641–1648
- [57] C. Reeb, C. Pierlot, C. A. Davy, D. Lambertin, Incorporation of organic liquids into geopolymer materials - A review of processing, properties and applications, *Ceram Int*, 2021, <https://doi.org/10.1016/j.ceramint.2020.11.239>.

- [58] L. Korat, V. Ducman, The influence of the stabilizing agent SDS on porosity development in alkali-activated fly-ash based foams *Cem. Concr. Compos.*, 80 (2017) 168-174
- [59] C. Bai, T. Ni, Q. Wang, H. Li, P. Colombo, Porosity, mechanical and insulating properties of geopolymer foams using vegetable oil as the stabilizing agent, *J. Eur. Ceram. Soc.* 38 (2018) 799–805
- [60] N. Thakur, C. A. Weatherly, R. M. Wimalasinghe, D. W. Armstrong, Fabrication of interconnected macroporosity in geopolymers via inverse suspension polymerization, *J Am Ceram Soc.* 102 (2019) 4405–4409
- [61] Y. C. Wang, J. P. Zhao, Comparative study on flame retardancy of silica fume-based geopolymer activated by different activators. *J. Alloys Compd.*, 743 (2018) 108-114
- [62] P. Tranchard, F. Samyn, S. Duquesne, M. Thomas, B. Estèbe, J.L. Montès JL, Fire behaviour of carbon fibre epoxy composite for aircraft: Novel test bench and experimental study, *J. Fire Sci.*, 33 (2015) 247-66
- [63] A. C. Kak, M. Slaney, *Principles of Computerized Tomographic Imaging*. IEEE Press, Piscataway, NJ, 1988
- [64] G. Peix, P. Duvauchelle, N. Freud, in *X-Ray Tomography in Material Science* (Hermes Science, London), 2000, Chap. 1:15–27
- [65] N. Limodin, T. Rougelot, J. Hosdez, 2013, <http://isis4d.univ-lille.fr/>
- [66] Y. Song, C. A. Davy, T. N. Kim, D. Troadec, G. Hauss, L. Jeannin, Two-scale analysis of a tight gas sandstone, *Phys Rev E* 94 (2016) 043316
- [67] J. Schindelin, I. Arganda-Carreras, E. Frise, V. Kaynig, M. Longair, T. Pietzsch T, Fiji: an open-source platform for biological-image analysis, *Nat Methods* 9(7) (2012) 676.
- [68] C. A. Davy, G. Hauss, B. Planel, D. Lambertin, 3D structure of oil droplets in hardened geopolymer emulsions, *J. Am. Ceram. Soc.*, (2018) 1–6

- [69] B. Münch, L. Holzer, Contradicting geometrical concepts in pore size analysis attained with electron microscopy and mercury intrusion, *J Am Ceram Soc.* 91(12) (2008) 4059–4067
- [70] V. F. F. Barbosa, K. J. D. MacKenzie, C. Thaumaturgo, Synthesis and Characterisation of Materials Based on Inorganic Polymers of Alumina and Silica: Sodium Polysialate Polymers, *Int. J. Inorg. Mater.*, 2(4) (2000) 309-317
- [71] M. R. Rowles, J. V. Hanna, K. J. Pike, M. E. Smith, B. H. O'Connor, ²⁹Si, ²⁷Al, ¹H and ²³Na MAS NMR study of the bonding character in aluminosilicate inorganic polymers, *Appl. Magn. Res.*, 32(4) (2007) 663-689
- [72] S. Greiser, P. Sturm, G. J. G. Gluth, M. Hunger, C. Jäger, Differentiation of the solid-state NMR signals of gel, zeolite phases and water species in geopolymer-zeolite composites, *Ceram. Int.* 43(2) (2017) 2202-2208
- [73] B. Walkley, R. San Nicolas, M. A. Sani, J. D. Gehman, J. S. J. Van Deventer, J. L. Provis, Phase evolution of Na₂O–Al₂O₃–SiO₂–H₂O gels in synthetic aluminosilicate binders, *Dalton Trans.*, 45(13) (2016) 5521-5535
- [74] D. Müller, G. Berger, I. Grunze, G. Ladwig, E. Hallas, U. Haubenreisser, Solid-state high-resolution ²⁷Al nuclear magnetic resonance studies of the structure of CaO–Al₂O₃–P₂O₅ glasses, *Phys. Chem. Glasses*, 24 (1983) 37–42
- [75] K. J. D. MacKenzie, M. E. Smith, A. Wong, A multinuclear MAS NMR study of calcium-containing inorganic polymers, *J Mater Chem.* 17(48) (2007) 5090-6
- [76] Y. Nie, M. Xia, S. Lu, ²⁹Si and ²⁷Al MAS-NMR studies of metakaolin changes during the polymerization of mineral polymer, *Appl. Mech. Mater.*, 543-544 (2014) 3818-3821
- [77] J. Rottstegge, M. Wilhelm, H. W. Spiess, Solid state NMR investigations on the role of organic admixtures on the hydration of cement pastes, *Cem. Concr. Compos.*, 28(5) (2006) 417-26

- [78] C. C. Liu, G. E. Maciel, The fumed silica surface: A study by NMR, *J Am Chem Soc.* 118(21) (1996) 5103-19
- [79] N. A. Jaya, L. Yun-Ming, H. Cheng-Yong, M. A. B. Abdullah, K. Hussin, Correlation between pore structure, compressive strength and thermal conductivity of porous metakaolin geopolymer, *Constr. Build. Mater.*, 247 (2020) 118641-
- [80] R.C. Progelhof, J.L. Throne, R.R. Ruetsch, Methods for predicting the thermal conductivity of composite systems: A review, *Polym. Eng. Sci.*, 16 (1976) 615-625.
- [81] F.L. Levy, A modified Maxwell-Eucken equation for calculating the thermal conductivity of two-component solutions or mixtures, *Int J Refrig*, 4 (1981) 223-225.
- [82] S. Kirkpatrick, Percolation and Conduction, *Reviews of Modern Physics*, 45 (1973) 574-588.
- [83] L. Gong, Y. Wang, X. Cheng, R. Zhang, H. Zhang, A novel effective medium theory for modelling the thermal conductivity of porous materials, *Int. J. Heat Mass Transfer*, 68 (2014) 295-298.
- [84] J. Wang, J.K. Carson, M.F. North, D.J. Cleland, A new approach to modelling the effective thermal conductivity of heterogeneous materials, *Int. J. Heat Mass Transfer*, 49 (2006) 3075-3083.
- [85] F. Xu, G. Gu, W. Zhang, H. Wang, X. Huang, J. Zhu, Pore structure analysis and properties evaluations of fly ash-based geopolymer foams by chemical foaming method, *Ceram. Int.*, 44 (2018) 19989-19997.
- [86] J.K. Carson, S.J. Lovatt, D.J. Tanner, A.C. Cleland, Thermal conductivity bounds for isotropic, porous materials, *Int. J. Heat Mass Transfer*, 48 (2005) 2150-2158.
- [87] H. Gao, L. Liao, H. Liu, L. Mei, Z. Wang, D. Huang, G. Lv, G. Zhu, and C. Wang, Optimization of thermal insulation performance of porous geopolymers under the guidance of thermal conductivity calculation, *Ceram. Int.*, 46[10] (2020) 16537-47.

- [88] R. H. Glaser, G. L. Wilkes, Structure property behavior of polydimethylsiloxane and poly(tetramethylene oxide) modified TEOS based sol–gel materials – V. Effect of titanium isopropoxide incorporation, *Polymer Bulletin* 19(1) (1988) 51–7
- [89] A. Samoson, E. Lippmaa, G. Engelhardt, U. Lohse, H. G. Jerschke, Quantitative high-resolution ²⁷Al NMR: tetrahedral non-framework aluminium in hydrothermally treated zeolites, *Chem Phys Lett.* 134(6) (1987) 589-92

Tables

	Oxide proportion (% wt)				Component mass (g +/-0.001)		
	Na ₂ O	Al ₂ O ₃	SiO ₂	H ₂ O	Reference GP	GP foam 1	GP foam 2
Metakaolin		40.16	54.09		46.957	46.957	46.949
Silica fume			96.76		28.073	28.076	28.079
Sodium silicate (Betol 39T)	8.3		27.5	64.2	67.403	67.402	67.402
Sodium hydroxide	77.5			22.5	7.570	7.569	7.569
H ₂ O ₂	-	-	-	-	0	3.015 (2%w)	3.002 (2%w)
CTABr	-	-	-	-	0	0	0.076 (0.05%w)
Total mass					150.003	153.019	153.077
Sample quantity					3	6	3

Table 1: Chemical composition of the components (obtained by X ray fluorescence) and composition of the GP foams formulated and tested in this research.

	Mass (g) after deposition	Mass (g) just before fire test	Mass loss due to curing (% initial mass)	Mass (g) after fire test	Mass loss after fire test (% mass before fire)	Total mass loss (% initial mass)	Coating thickness (mm) without steel plate	Maximum temperature (°C) (and temperature difference compared to uncoated steel plate)
Ref. GP	40.4 +/-1.2	31.5 +/-1.2	-22	25.2 +/-1.2	-20.0	-38.0	3.2 +/-0.3	513 (-122)
GP Foam 1	41.5 +/-1.2	38.7 +/-1.2	-7.0	27.3 +/-1.2	-29.0	-34.0	5.5 +/-0.3	432 (-203)
GP Foam 2	41.4 +/-1.2	40.5 +/-1.2	-2.1	27.9 +/-1.2	-31.0	-32.5	10.7 +/-4.4	384 (-251)

Table 2: Mass loss, thickness and maximum temperature of GP coatings before and after fire test at 7 days curing. Steel plate alone reaches a maximum temperature of 640°C +/-5.

Position (ppm)	-80	-88	-93	-98	-103	-107	-110	
Site	Q ⁴ (4Al)	Q ⁴ (3Al)	Q ⁴ (2Al)	Q ⁴ (1Al)	Q ⁴ (MK)	Q ⁴ (Quartz)	Q ⁴ (SF)	GP
	(%)							
Reference GP before fire	0.5	12.3	23.6	32.1	16.6	3.6	11.3	68.5
Reference GP after fire	0.0	7.5	21.1	29.4	21.5	2.6	17.9	58.0
GP foam n.1 before fire	0.0	11.5	22.4	26.3	28.5	1.4	9.9	60.2
GP foam n.1 after fire	0.0	7.4	18.3	28.2	30.3	2.1	13.6	53.9
GP foam n.2 before fire	1.7	15.7	26.2	22.6	20.1	2.0	11.8	66.1
GP foam n.2 after fire	0.0	13.1	20.4	19.4	31.3	1.6	14.2	52.9

Table 3: Deconvolution results of ²⁹Si MAS NMR spectra before and after fire test. GP is the sum of the proportions of Q⁴(4Al), Q⁴(3Al), Q⁴(2Al) and Q⁴(1Al) sites, attributed to the GP polymeric network.

	Sample size (voxels³)	Sample size (mm³)	Porosity	Main pore size d₅₀ (mm)
Reference GP at 7 days before fire test	750x329x520	39.5	24.5	0.49
Reference GP at 7 days after fire test	784x215x771	40.0	30.0	0.23
GP foam n.1 at 7 days before fire test	451x686x313	30.0	30.0	0.63
GP foam n.1 at 7 days after fire test	438x404x481	26.2	40.7	0.43
GP foam n.2 at 7 days before fire test	514x432x935	63.8	81.0	3.02
GP foam n.2 at 7 days after fire test	500x500x800	61.5	79.6	2.65

Table 4: 3D X ray micro-CT - Sample characteristics and main results (porosity and pore diameter d₅₀ at half the cumulative pore size distribution).

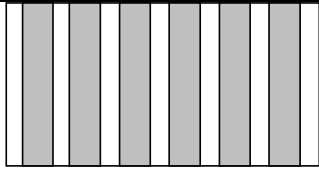
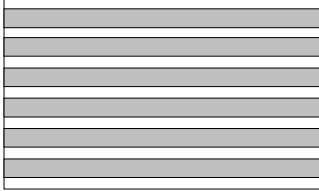
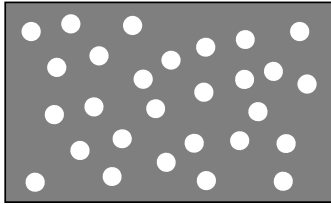
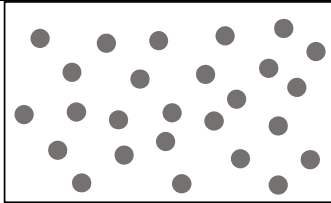
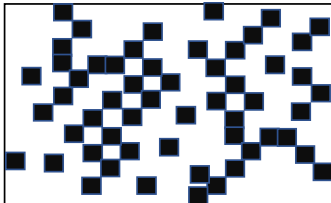
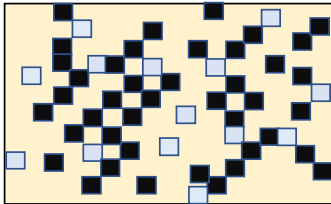
Model	Schematic structure	Effective heat conduction equation
<i>Parallel</i>		$k_e = (1 - \varepsilon)k_s + \varepsilon k_f$
<i>Series</i>		$k_e = \frac{1}{\frac{(1 - \varepsilon)}{k_s} + \frac{\varepsilon}{k_f}}$
<i>Maxwell – Eucken form 1</i> ($k_s = \text{continuous phase}$; $k_f = \text{dispersed phase}$)		$k_e = k_s \frac{2k_s + k_f - 2(k_s - k_f)\varepsilon}{2k_s + k_f + (k_s - k_f)\varepsilon}$
<i>Maxwell – Eucken form 2</i> ($k_s = \text{dispersed phase}$; $k_f = \text{continuous phase}$)		$k_e = k_f \frac{2k_f + k_s - 2(k_f - k_s)(1 - \varepsilon)}{2k_f + k_s + (k_f - k_s)(1 - \varepsilon)}$
<i>EMT</i>		$k_e = \frac{1}{4} \left[k_f(3\varepsilon - 1) + k_s(3(1 - \varepsilon) - 1) \right] + \sqrt{\left[(3\varepsilon - 1)k_f + (3(1 - \varepsilon) - 1)k_s \right]^2 + \dots}$
<i>NEMT</i>		$k_e = \frac{k_s(1 - \varepsilon)(k_f + 2k_m) + k_f\varepsilon(k_s + 2k_n)}{\varepsilon(k_s + 2k_m) + (1 - \varepsilon)(k_f + 2k_m)}$

Table 5: Description and calculation of the effective heat conductivity for two-components materials based on 6 structural models (adapted from [78]) – k_e is the effective heat conductivity, k_s is the heat conductivity of the solid, k_f is the heat conductivity of the fluid and ε is porosity

Fire exposure	Geopolymer	Porosity	k_{exp} (W/(m.K))	k_e (W/(m.K))	k_m (W/(m.K))	
Before testing	Ref GP	0.25	0.26	Parallel:	0.65	-
				Series:	0.10	-
				Maxwell-Eucken 1:	0.58	-
				Maxwell-Eucken 2:	0.20	-
				EMT:	0.55	-
				NEMT:	0.26	0.05
	GP foam 1	0.30	0.30	Parallel:	0.60	-
				Series:	0.08	-
				Maxwell-Eucken 1:	0.53	-
				Maxwell-Eucken 2:	0.16	-
				EMT:	0.49	-
				NEMT:	0.30	0.10
	GP foam 2	0.81	0.18	Parallel:	0.18	-
				Series:	0.03	-
				Maxwell-Eucken 1:	0.14	-
				Maxwell-Eucken 2:	0.04	-
				EMT:	0.05	-
				NEMT:	0.18	15.0
After testing	Ref GP	0.30	0.27	Parallel:	0.60	-
				Series:	0.08	-
				Maxwell-Eucken 1:	0.53	-
				Maxwell-Eucken 2:	0.17	-
				EMT:	0.49	-
				NEMT:	0.27	0.08
	GP Foam 1	0.41	0.14	Parallel:	0.51	-
				Series:	0.06	-
				Maxwell-Eucken 1:	0.43	-
				Maxwell-Eucken 2:	0.12	-
				EMT:	0.36	-
				NEMT:	0.14	0.04
	GP Foam 2	0.80	0.09	Parallel:	0.19	-
				Series:	0.03	-
				Maxwell-Eucken 1:	0.15	-
				Maxwell-Eucken 2:	0.04	-
				EMT:	0.05	-
				NEMT:	0.09	0.17

Table 6: Experimental thermal conductivity (k_{exp}) and effective thermal conductivity (k_e) calculated according to the six basic structural models of the geopolymer before and after fire testing; thermal conductivity k_m provided by the NEMT model is also provided.

Figures

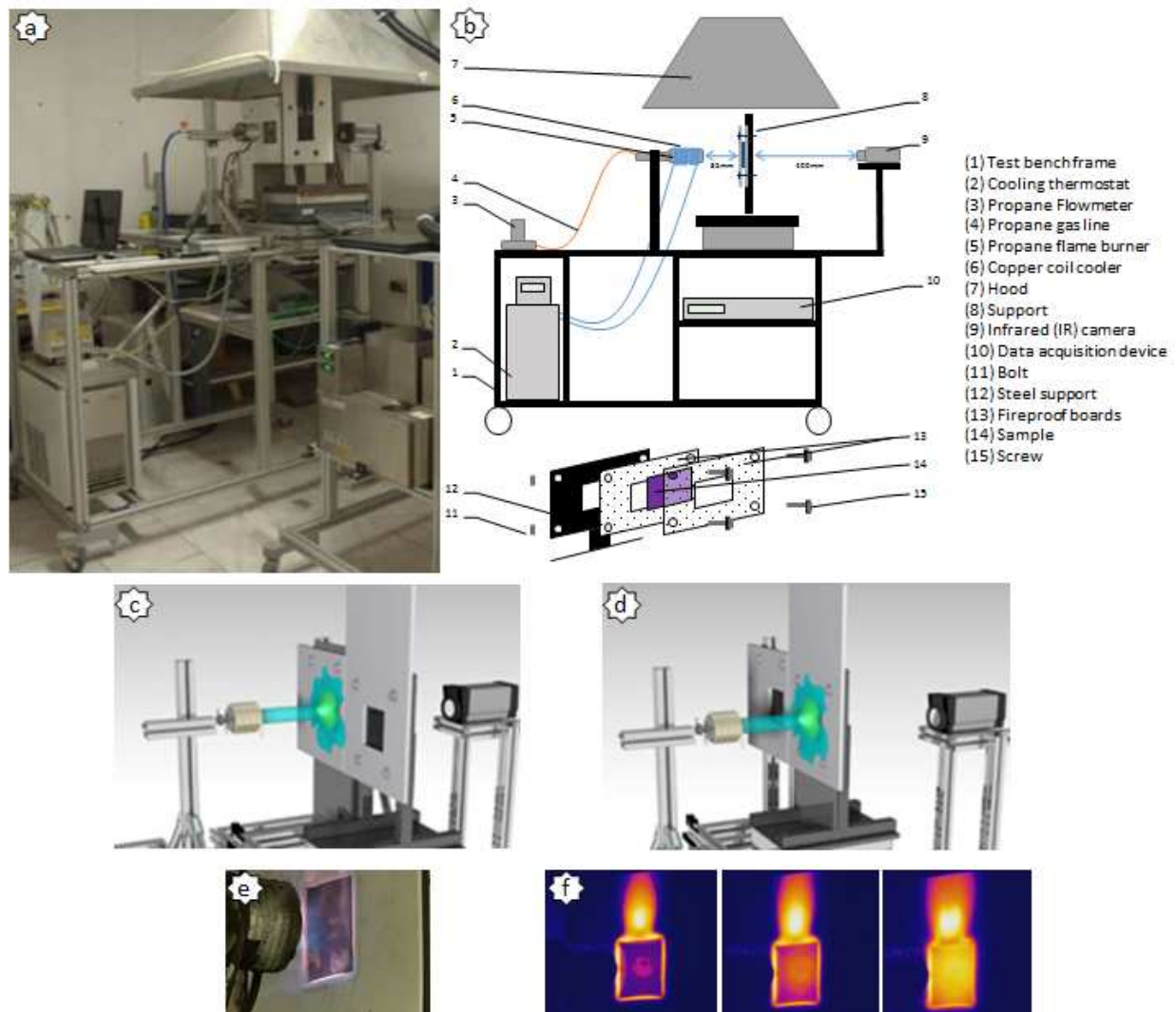


Figure 1: Description of the burn-through fire test set-up; (a): photograph of the test bench; (b): different elements of the test bench; (c): calibration with water-cooled calorimeter; (d): fire test on a coated steel plate; (e): close-up of the propane flame burner directly heating the coated plate; (f): Evolution of heating through the flame observed with the IR camera placed in front of the sample.

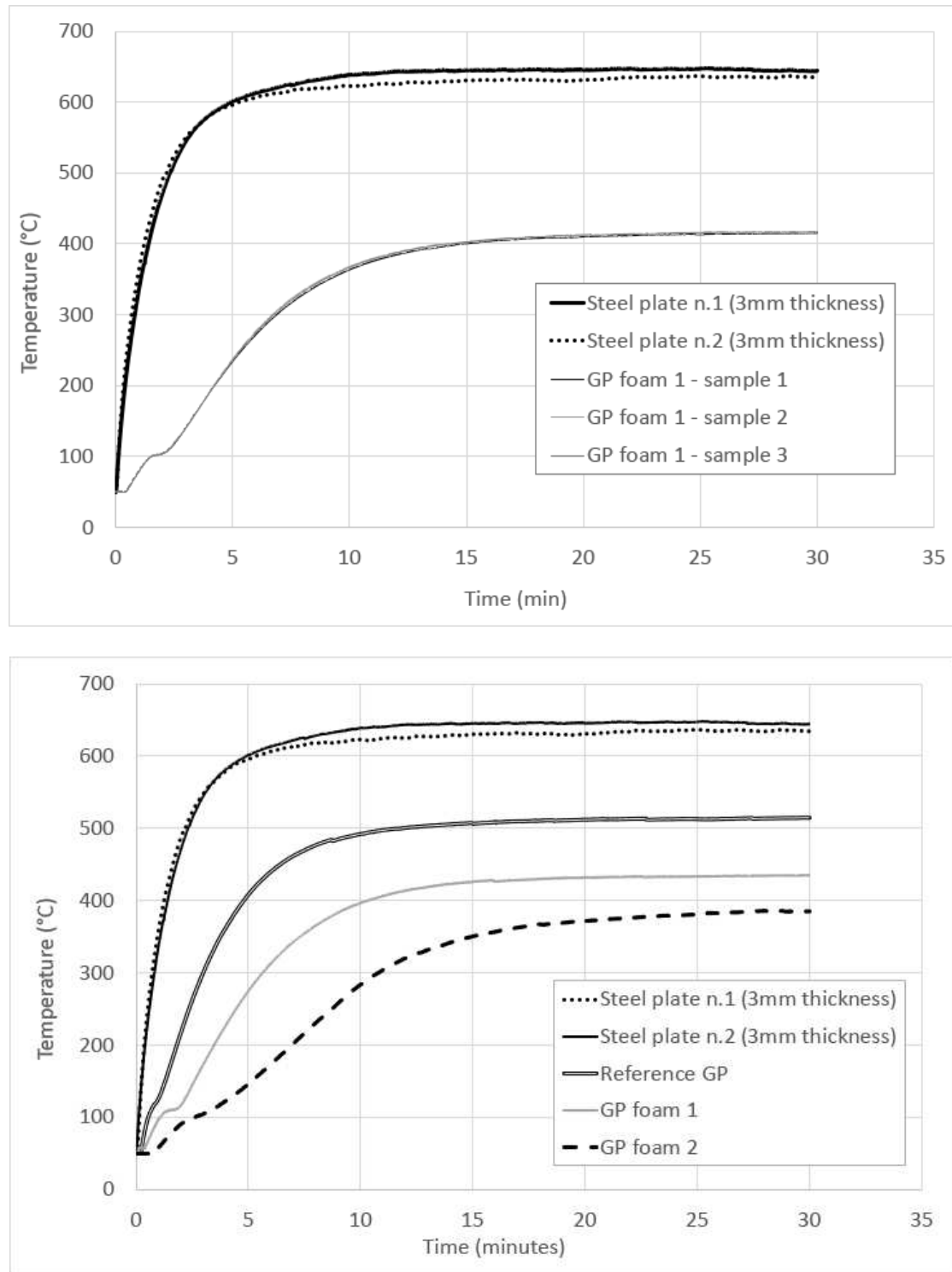


Figure 2: (a): Repeatability results for burn-through fire test on steel plate alone (two samples) and on GP foam 1 (three distinct samples): temperature profiles versus time; (b): Burn through test results for the three foam formulations after 7 days curing: temperature profiles as a function of time, compared to two samples of steel plate alone (reaching a maximum temperature of 640°C +/-5).

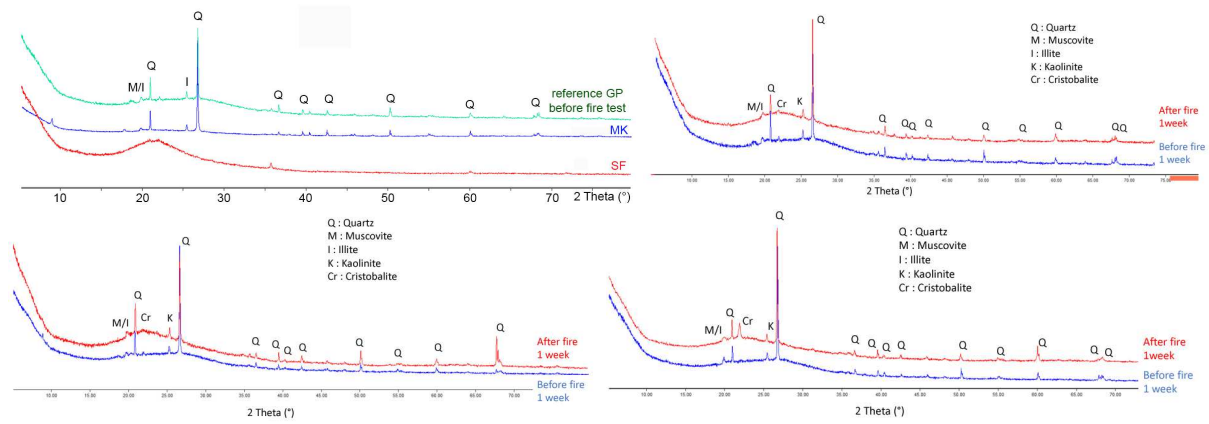


Figure 3: XRD results for (top left): raw silica fume (in red), metakaolin powder (in blue) compared to reference GP (in green) at 7 days maturation, and before fire test (in blue) and after fire test (in red) for (top right): reference GP; (bottom left) GP foam 1 and (bottom right) GP foam 2. Q stands for quartz, M for muscovite, I for illite, K for kaolinite and Cr for cristobalite.

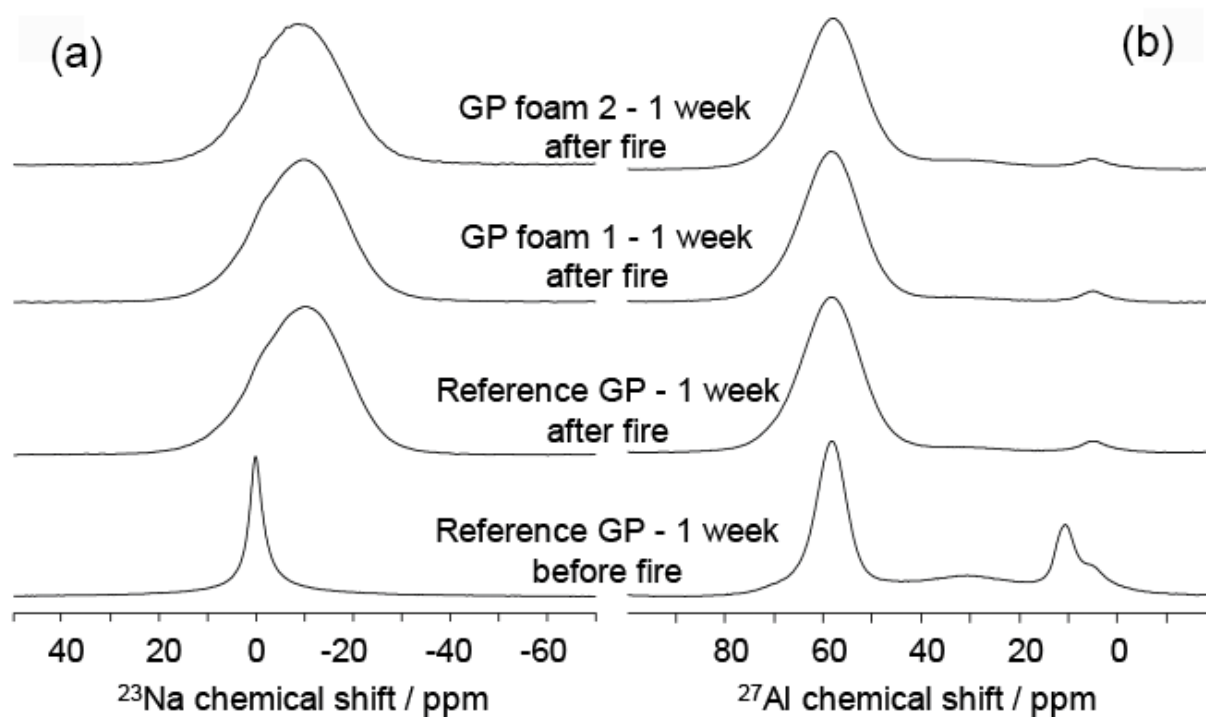


Figure 4: Solid state MAS NMR: (a): ^{23}Na and (b): ^{27}Al spectra for reference GP before and after fire, compared to GP foams n.1 and n.2 after fire.

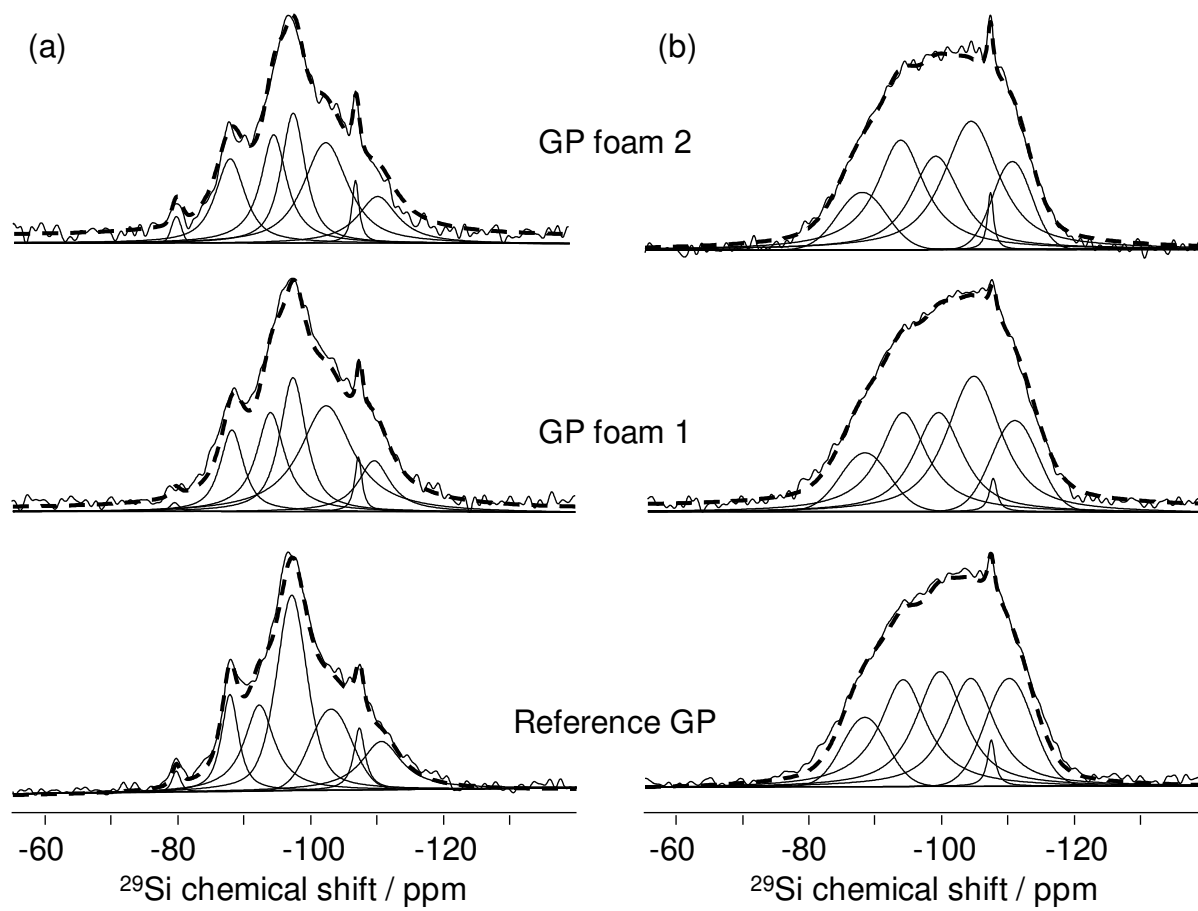


Figure 5: ^{29}Si MAS NMR spectra for reference GP, GP foams 1 and 2, before fire test : (a) column, and after fire test : (b).


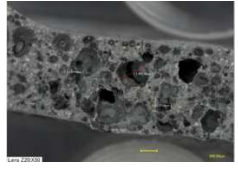

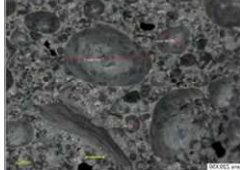



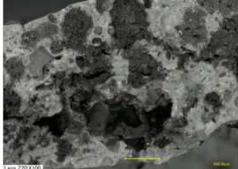




Material	Reference GP	GP foam 1	GP foam 2
<p>After 7 days maturation and before fire test</p> <p>(top: no magnification; bottom: x500)</p>	 	 	 
<p>After 7 days maturation and after fire test</p> <p>(top: no magnification; bottom: x500)</p>	 	 	 

Figure 6: Macrophotographs of GP foam coatings before and after fire test.

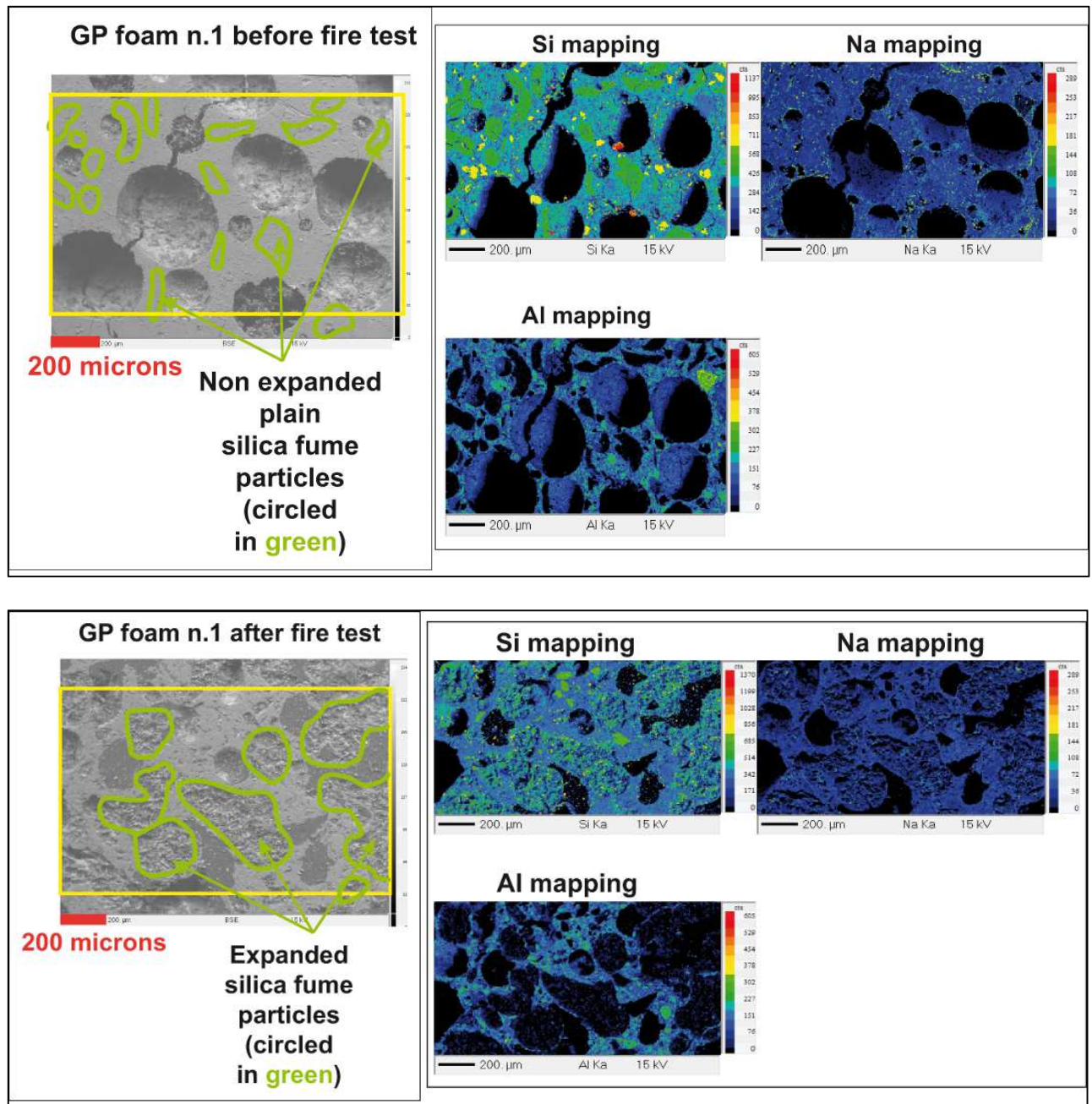


Figure 7: Results of electron probe micro-analysis for GP foam n.1: (top): before fire test and (bottom): after fire test, showing expanded silica fume particles after fire test only. Similar results are obtained with reference GP and GP foam n.2.

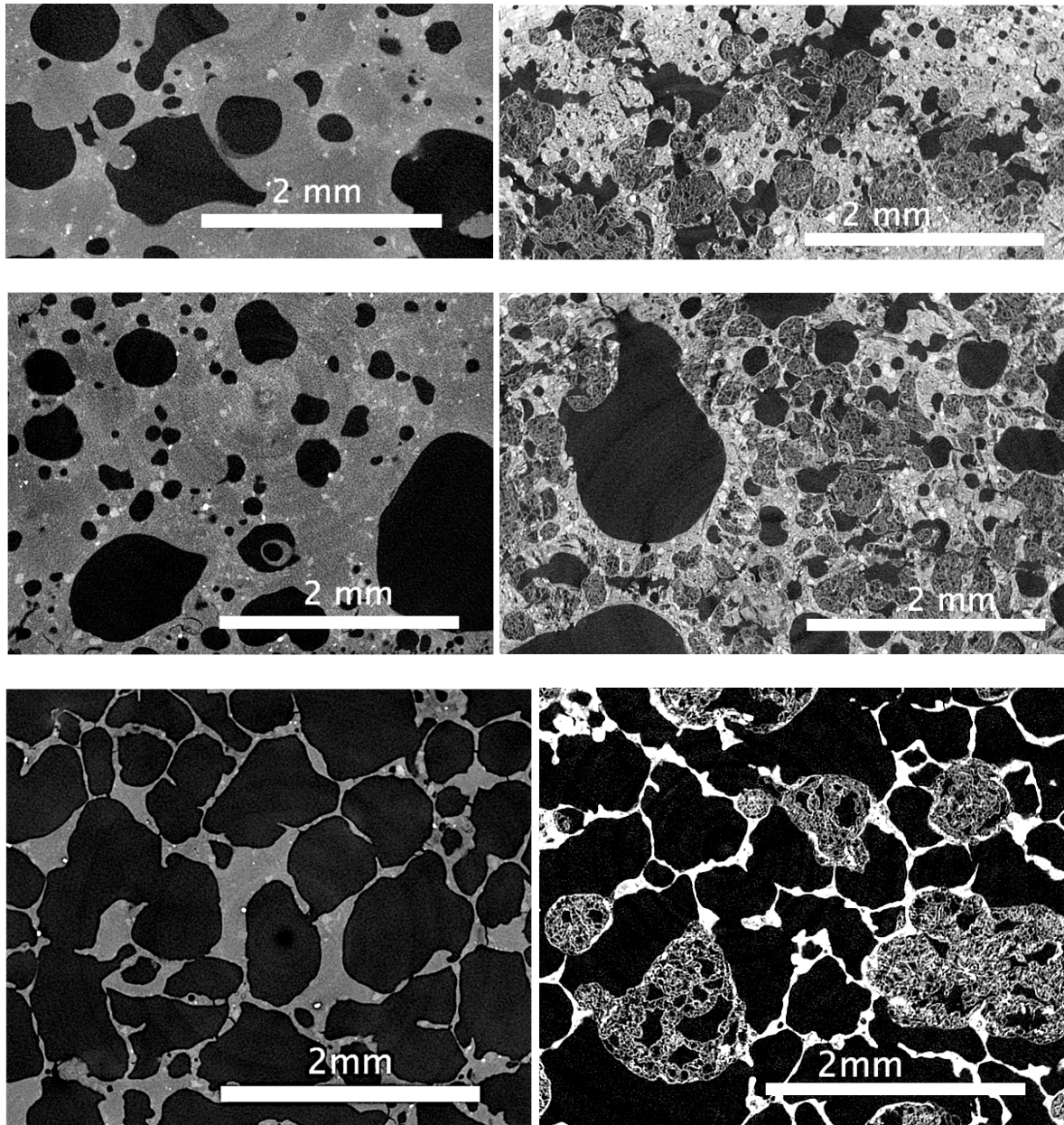


Figure 8: Close-ups of typical grey level X ray micro-CT images before fire test (left column) and after fire test (right column) after 7 days curing; The images correspond to: (top) reference GP, (middle) GP foam n.1 and (bottom) GP foam n.2. Pores are in black and the GP solids are in various grey values. Silica fume grains appear in darker grey (they are clearly highly porous after fire), and MK particles are in the lightest grey value.

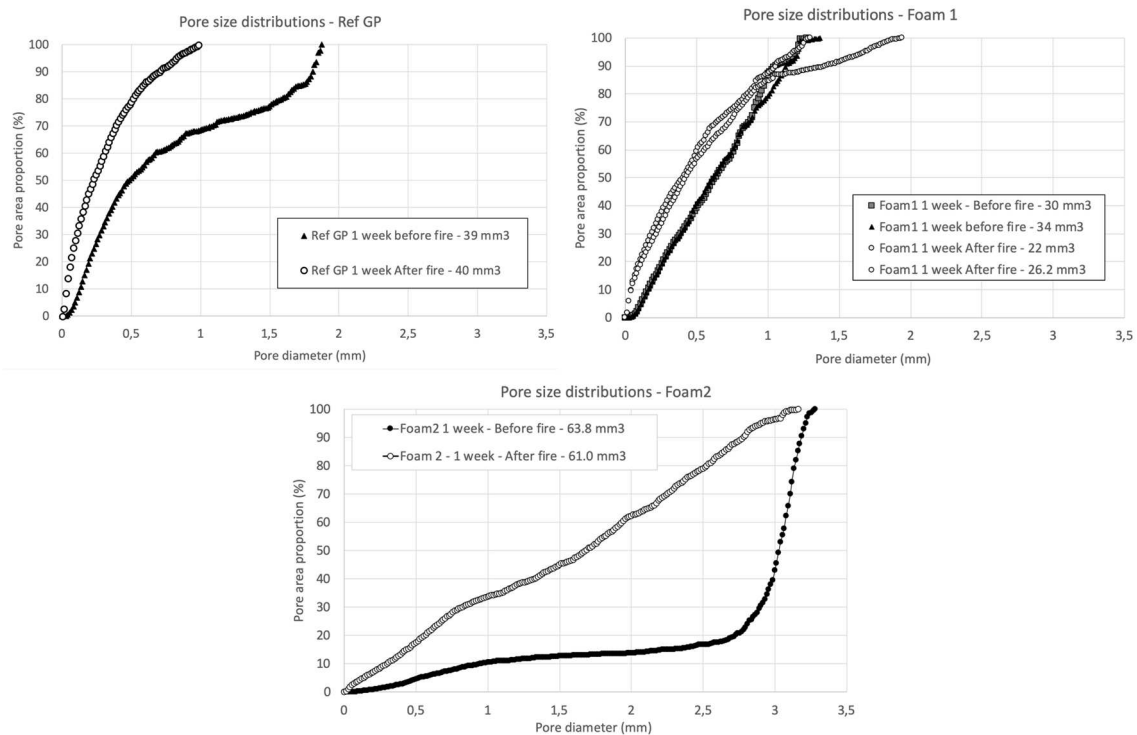


Figure 9: X ray micro-CT results (before and after fire test) at 7 days - pore size distributions for reference GP (top left), GP foam n.1 (top right) and GP foam n.2 (bottom). The volumes analyzed for each samples are provided in the legend.

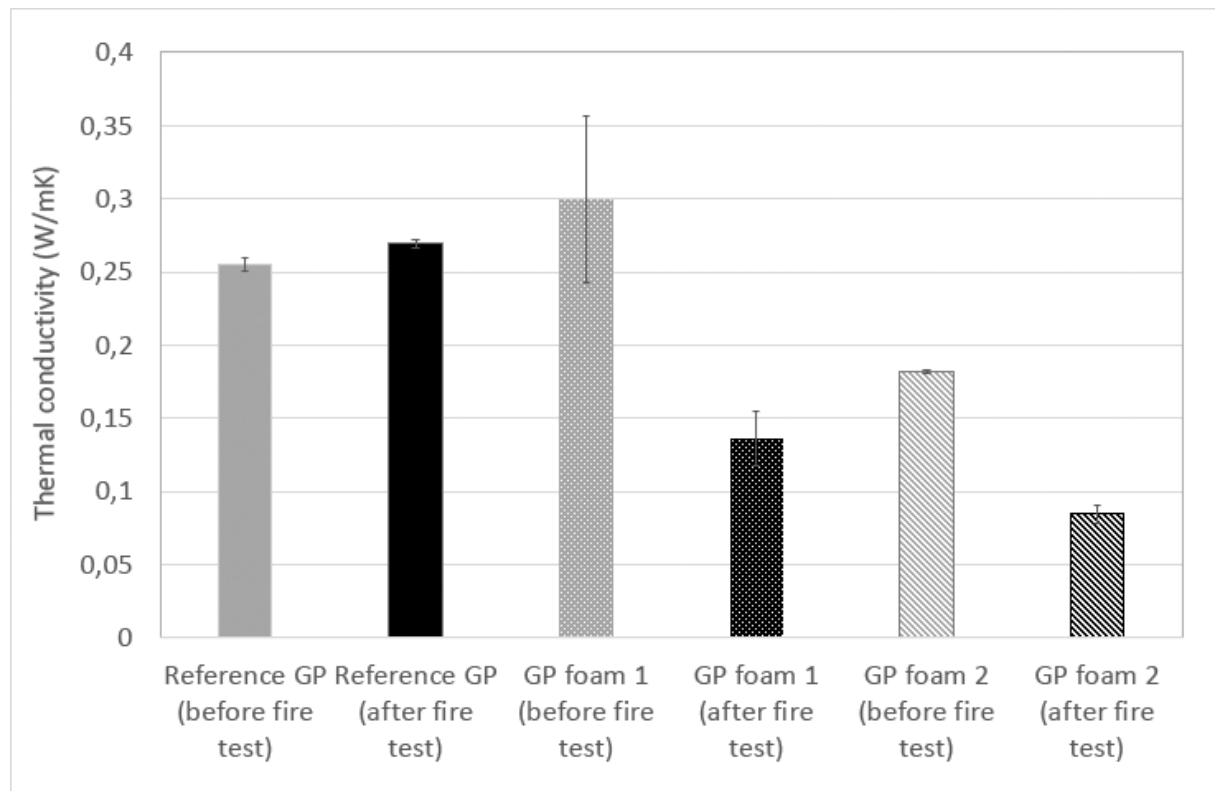


Figure 10: Thermal conductimetry results before and after fire test for reference GP and GP foams 1 and 2. All GP coatings are cured for 7 days.

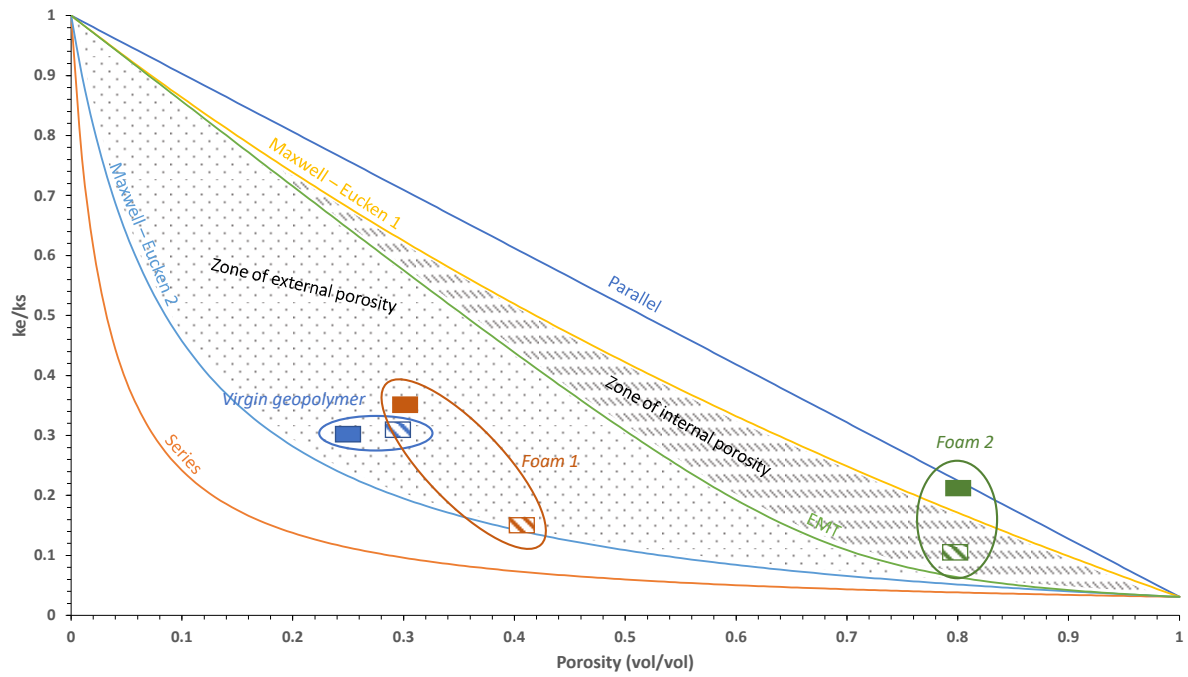


Figure 11: Ratio (k_e/k_s) as a function of porosity for five structural models indicating the zones of internal and external porosity and experimental thermal conductivity of the geopolymers (plain square: before fire testing – hatched square: after fire testing)